

INHOMOGENEITIES AND DEVITRIFICATION IN FUSED GLASS
SPECIMENS FABRICATED BY PULSED ELECTRIC CURRENT SINTERING
OF FUMED SILICA NANOPARTICLES

BY

FIONA RUTH CORMACK

A THESIS PRESENTED TO THE FACULTY OF

ALFRED UNIVERSITY

IN PARTIAL FULFILLMENT OF THE REQUIREMENTS
FOR THE DEGREE OF

DOCTOR OF PHILOSOPHY

IN

GLASS SCIENCE

ALFRED, NY

SEPTEMBER 2018

INHOMOGENEITIES AND DEVITRIFICATION IN FUSED GLASS
SPECIMENS FABRICATED BY PULSED ELECTRIC CURRENT SINTERING
OF FUMED SILICA NANOPARTICLES

BY

FIONA RUTH CORMACK

B.S. CARNEGIE MELLON UNIVERSITY (2010)

SIGNATURE OF AUTHOR _____

APPROVED BY _____
ALEXIS CLARE, ADVISOR

WILLIAM LACOURSE, ADVISORY COMMITTEE

PAUL F. JOHNSON, ADVISORY COMMITTEE

HOLLY SCHULMAN, ADVISORY COMMITTEE

CHAIR, ORAL THESIS DEFENSE

ACCEPTED BY _____
ALASTAIR CORMACK, DEAN
KAZUO INAMORI SCHOOL OF ENGINEERING
ALFRED UNIVERSITY

ACCEPTED BY _____
JAY CERIO, DEAN
GRADUATE AND CONTINUING STUDIES
ALFRED UNIVERSITY

Alfred University theses are copyright protected and may be used for education or personal research only. Reproduction or distribution in part or whole is prohibited without written permission from the author.

Signature page may be viewed at Scholes Library, New York State College of Ceramics, Alfred University, Alfred, New York.

ACKNOWLEDGEMENTS

"The best laid schemes o' Mice an' Men, / Gang aft agley,"

- Robert Burns

When I think about all the projects I've been a part of during my years at Alfred University, it's funny to observe that this is the one that became the subject of my thesis. When I did most of the work presented here, I was investigating a completely different topic and this content was meant to be a small (dare I say "trivial"?) piece of that puzzle. I think you can guess how that worked out in the end. I considered formatting this thesis as a "choose your own adventure" story to more accurately represent the convoluted path that research can take, especially when one is starting from scratch, but finally opted for a more traditional approach. In the end, I'm escaping with some of my sanity remaining. I'd like to acknowledge all the forces of nature that both helped and hindered me along the way, and so many people that were also part of this odyssey. Cheers, guys.

TABLE OF CONTENTS

| | |
|--|-----|
| ACKNOWLEDGEMENTS..... | iii |
| TABLE OF CONTENTS..... | iii |
| LIST OF TABLES..... | vi |
| LIST OF FIGURES..... | vii |
| ABSTRACT..... | x |
| I. INTRODUCTION..... | 1 |
| II. BACKGROUND INFORMATION..... | 3 |
| A. Fumed Silica..... | 3 |
| B. Sintering of Amorphous Silica..... | 4 |
| C. Devitrification During Sintering..... | 5 |
| D. Silica Crystallization Kinetics..... | 8 |
| E. Pulsed Electric Current Sintering..... | 13 |
| F. On the Presence of Plasma..... | 14 |
| G. Known Issues and Challenges..... | 14 |
| III. LITERATURE REVIEW..... | 18 |
| IV. EXPERIMENTAL PROCEDURE..... | 21 |
| A. Considerations Regarding Silica Volatilization in Reducing Conditions and Reactions Between SiO ₂ and Graphite..... | 23 |
| V. RESULTS AND DISCUSSION..... | 30 |
| A. Inherent Variability of Results According to the Experimental Set-up..... | 32 |
| B. Graded Porosity in Glass Scaffolds Fabricated via Pulsed Electric Current Sintering of Fumed Silica Nanoparticles at Temperatures ≤ 900 °C..... | 35 |
| C. Rapid Fabrication of Fused Glass Specimens Using Pulsed Electric Current Sintering of Amorphous Fumed Silica Nanoparticles..... | 51 |

| | | |
|------|--|----|
| D. | On the Effect of Pressing Force on Consolidation of Fumed Silica Powder using Pulsed Electric Current Sintering | 65 |
| E. | Rapid Devitrification of Silica Glass During PECS..... | 70 |
| VI. | CONCLUSIONS AND FUTURE WORK..... | 80 |
| VII. | REFERENCES | 82 |

LIST OF TABLES

| | | |
|-------------------|--|----|
| Table I: | Properties of Aerosil OX50. | 25 |
| Table II: | FTIR Absorbance Band and Sub-band Assignments..... | 27 |
| Table III: | Experimental Parameters. | 28 |
| Table IV: | Tabulated Data for the Rietveld Refinement (TOPAS) and DIFFaX Analysis..... | 79 |

LIST OF FIGURES

| | | |
|-------------------|---|----|
| Figure 1: | SEM images of Aerosil fumed silica.. | 6 |
| Figure 2: | HRTEM images of Aerosil fumed silica aggregate particles. | 7 |
| Figure 3: | Silica phase diagram.. | 10 |
| Figure 4: | The high and low temperature forms of cristobalite | 11 |
| Figure 5: | General schematics of (a) Time-temperature-transformation (TTT) diagram for crystallization of amorphous silica, and (b) pathways for devitrification and densification during sintering..... | 12 |
| Figure 6: | Experimental set-up for PECS processing..... | 16 |
| Figure 7: | Comparisons of (a) current density and (b) temperature variation through the die ensemble for electrically insulating and conducting samples. (c) Shows the different temperatures measured by optical pyrometer and a thermocouple inserted into the die wall of the same sample | 17 |
| Figure 8: | Fitted FTIR Spectrum for Aerosil OX 50 (aged/hydrated)..... | 26 |
| Figure 9: | Example PECS program. | 29 |
| Figure 10: | Variation in measured shrinkage with heating for samples heated to 800 °C at 100 °C/min.. | 34 |
| Figure 11: | Sample PECS program output. | 38 |
| Figure 12: | Optical micrograph of a typical intermediately sintered SiO ₂ porous compact..... | 39 |
| Figure 13: | Characteristic consolidation visualized as piston position plotted against temperature.. | 40 |
| Figure 14: | Final piston position vs maximum external die wall temperature. | 41 |

| | | |
|-------------------|---|----|
| Figure 15: | Fitted FTIR Spectrum for Aerosil sintered at 800 °C.. | 42 |
| Figure 16: | Cumulative pore volume as estimated via gas adsorption testing vs. estimated pore volume from PECS final relative piston position..... | 43 |
| Figure 17: | SEM micrographs of sintered microstructure. | 44 |
| Figure 18: | Comparison of N ₂ Gas Adsorption Isotherms for Aerosil OX50, and samples processed via PECS to 800 °C with heating rates of 100 °C/min and 200 °C/min. | 45 |
| Figure 19: | Comparison of N ₂ gas adsorption Isotherms for samples sintered at 500 °C, 700 °C, and 900 °C, with a heating rate of 150 °C/min.. | 46 |
| Figure 20: | Dollimore-Heale pore distributions; 150 °C/min to (a) 500 °C, no hold (b) 700 °C, no hold (c) 900 °C, no hold | 47 |
| Figure 21: | Dollimore-Heale pore distributions vs. heating rate (d) 200 °C/min to 800 °C, 5 minute hold (e) 100 °C/min to 800 °C, 5 minute hold (f) as received (un-sintered). | 48 |
| Figure 22: | Mean and median pore widths with sintering temperature.. | 49 |
| Figure 23: | Mean and median pore widths with hold time at max. temperature. | 50 |
| Figure 24: | Characteristic consolidation visualized as piston position plotted against temperature.. | 53 |
| Figure 25: | Final relative piston position vs. maximum sintering temperature..... | 54 |
| Figure 26: | Fitted FTIR Spectrum for Aerosil sintered at 1100 °C..... | 55 |
| Figure 27: | Optical micrographs of samples heated to (a) 1000 °C (b) 980 °C (c) 940 °C..... | 57 |
| Figure 28: | SEM micrographs of sample fracture surfaces etched in 17% HF for 24 hours | 58 |

| | | |
|-------------------|---|----|
| Figure 29: | Voids and texture at fracture surface between glassy and crystalline phase. (a) SEM micrograph; (b) Composite optical micrograph..... | 59 |
| Figure 30: | Examples of common macroscopic defects in fused glass specimens. | 60 |
| Figure 31: | Ranking system for flaws in samples..... | 61 |
| Figure 32: | Frequency and extensivity of flaws, and correlation of flaws with heating rate..... | 64 |
| Figure 33: | Schematic of the progression of the fusion front into the glass powder compact..... | 64 |
| Figure 34: | Optical micrographs of PECS samples..... | 67 |
| Figure 35: | Characteristic consolidation visualized as piston position plotted against temperature.. | 68 |
| Figure 36: | Pressing force vs. onset of sintering and complete consolidation temperatures..... | 69 |
| Figure 37: | Optical micrographs with examples of (a) bulk and (b) edge devitrification..... | 71 |
| Figure 38: | SEM images of fracture surfaces showcasing cristobalite with an unusual, cross-hatched microstructure texture..... | 72 |
| Figure 39: | Schematic of devitrified glass and experimental XRD sample configuration and orientation..... | 73 |
| Figure 40: | X-ray diffractograms for (a) a chunk of bulk crystalline material (b) crystalline sample that has been pulverized to remove effects of directional growth. Cristobalite planar reflection peaks are labeled. | 74 |
| Figure 41: | Rietveld refinement of α -cristobalite diffraction profile confirms phase identification (top) ($R_{wp} = 27\%$) | 77 |
| Figure 42: | Hand-optimized diffraction profile of the α -cristobalite (011) peak shows evidence for stacking disorder in the low-angle shoulder | 78 |

ABSTRACT

An investigation of the feasibility of rapidly producing fused silica glass parts from powder compacts using Pulsed Electric Current Sintering was carried out. This sintering method was found to be inherently non-isothermal and inhomogeneous, specifically when processing electrically-insulating glass samples. It was evident that significant temperature variation within the die ensemble does not equilibrate during the time the sample is being processed. Amorphous silica powder compacts fused according to the thermal gradients within the die ensemble, resulting in an axially graded porous microstructure for intermediately sintered samples, and extensive macroscopic defects (trapped bubbles, devitrification) in nominally fully consolidated glass parts. The results of this study indicate that in order to consistently attain a pristine amorphous silica part using Pulsed Electric Current Sintering, extreme care must be taken to avoid significant thermal gradients within the die ensemble, thus identifying future design challenges in this area.

I. INTRODUCTION

Fused silica glass is used regularly for a large variety of applications, most of which exploit its wide transparency range, mechanical strength, thermal and chemical stability, and low coefficient of thermal expansion. It is commonly used for optical fiber, lenses, mirrors, and substrate material. Additionally, porous amorphous silica has a myriad of exploitable characteristics derived from its microstructure and the superior thermal and optical properties of silica itself. Continuous porosity can allow capillary transport of liquids and diffusion of gases. Amorphous silica has a wide transparency range, extending from the UV to the near IR, and porous monoliths can transmit diffuse light, unlike similar polycrystalline refractory materials, such as alumina. Porous silica parts can be fused directly to fully dense glass, allowing for fabrication of composite components.

Traditional casting of silica glass parts is energy intensive, as silica has a high glass transition temperature requiring the melt temperature to be at or above 1650 °C. It is difficult to avoid introduction of impurities into the glass melt, compromising high-purity processes. Further, only fully dense parts can be fabricated this way, and the complexity of shapes that can be easily made is limited.

Sol-gel synthesis routes are often utilized to obtain highly pure amorphous silica parts, especially for the creation of optical devices, such as lenses and fiber. Using a low temperature approach is much less energy intensive than melting and casting glass parts. However, fabricating dense, monolithic samples via this route takes a very long time, on the order of months, and requires additional drying agents and careful humidity control to avoid fracture of the part as water leaves the sample.

Another path to silica monoliths is via sintering of a powder. With traditional sintering, the pore size and distribution can be controlled by adjusting the particle size of the powder and sintering parameters, allowing for microstructure control. The time required to fabricate parts this way is also significant, although it is much faster than drying and sintering a part from a gel.

An alternative to conventional sintering is “Pulsed Electric Current Sintering” (PECS), colloquially referred to as “Spark Plasma Sintering” (SPS), is a sintering technique that utilizes an axial pressing force and pulsed direct electrical current. Joule heating is produced by passing current through a conductive die containing the powder sample, allowing for very fast heating and cooling rates.

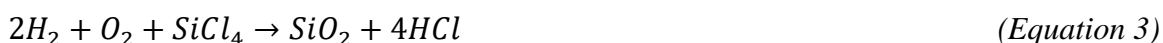
Achieving high density samples at lower temperatures and/or shorter processing times is practically and economically beneficial, so it is logical to investigate the feasibility of rapidly fabricating fused silica glass parts this way. To date, application of PECS to glass samples has been very limited. A summary and discussion of these published studies is given in the Literature Review, and the variety of results implies that it is non-trivial to obtain reproducible results when sintering a glass powder. At the least, experimental parameters are not reported completely and consistently

In this study, an amorphous fumed silica nanopowder is sintered using PECS to produce both porous and fully consolidated glass samples.

II. BACKGROUND INFORMATION

A. Fumed Silica

Fumed silica, sometimes referred to as pyrogenic silica, is the product created by flame pyrolysis of silicon tetrachloride via the reactions given in Equations 1 and 2, with the overall reaction summarized in Equation 3:



The amorphous nanopowder product is of highest purity as the only contaminant from this route of synthesis is residual chlorine, which is easy to remove. If left untreated, the fumed silica powder will tend to form aggregates that will then agglomerate due to interparticle interactions. Additionally, virgin fumed silica will react with atmospheric moisture to form hydroxyl groups until the available surface area is saturated. If left stored for extended periods, not only will fumed silica contain a significant amount of water, but particles in contact with each other may also bond together permanently as hydroxyl groups condense and reform siloxane bonds:



Scanning and transmission electron microscopy (SEM and TEM, respectively) images from Evonik¹ (Figures 1, 2) show examples of aggregates and agglomerates of fumed silica, respectively. In Figure 2, the high resolution TEM (HRTEM) microscopy clearly shows the fusion of the individual particles in the agglomerate. Many commercially available fumed silica products are treated to add hydrophobic surface groups which prevent aggregation, hydration, and hydrothermal “cold sintering.”

B. Sintering of Amorphous Silica

The initial stage of sintering is characterized by neck growth at contact points between particles that is driven by the reduction of curvature between the surfaces. This stage accounts for linear shrinkage of 3-5%, which corresponds to neck radius of about 0.4-0.5 of the particle radius. A compact is considered to have reached an intermediate stage of sintering when the pore shape has reached an equilibrium according to surface and interfacial tensions. From here, sintering proceeds via reduction in cross-section of the continuous pore network until isolated pores are formed. At this point the compact will have reached about 90% of the theoretical density.

Sintering of amorphous silica has, of course, been studied both theoretically and experimentally. Densification during sintering occurs by viscous flow, and sintering occurs near to the glass transition temperature. The geometrical models of Scherer²⁻⁵, and Mackenzie and Shuttleworth⁶ for densification of amorphous materials are generally considered to be valid for the intermediate and late stages of sintering. In this case, the energy required for viscous flow is equal to that gained by the reduction of surface area of the material. The rate of viscous sintering is inversely proportional to the viscosity of the glass (η), so the extent of densification after a time t is proportional to t/η , noting that η is a function of temperature. Nearly all sintering models assume isothermal conditions, and do not account for densification that occurs during sample heating or cooling, or if a thermal gradient is present. Qualitatively, a faster heating rate should result in a higher temperature necessary to complete densification, as the glass has less time flow at a given temperature.

Numerical approaches, including finite element analyses, have been developed to model the sintering process which generally agree with the accepted geometric models and experimental data.⁷⁻¹⁰ Unfortunately, the complexity of the simulations does not allow for disambiguation of the effect of key parameters on sintering kinetics. A phenomenological approach, in which data is collected and analyzed empirically, is the most common way to predict the sintering behavior of a material under normal conditions.¹¹

C. Devitrification During Sintering

Bulk densification of a glass compact depends on viscous flow, but crystallization depends on two kinetic steps: nucleation and growth. Nucleation is dependent on viscosity, but also on undercooling. Therefore, increasing the heating rate at temperatures where nucleation is fast can delay the onset of crystallization. Crystallization of silica has been shown to be suppressed by a reducing environment, likely due to an increased number of oxygen vacancies.¹²⁻¹⁵

Crystallization and sintering can occur in sequence, simultaneously, or some combination of the two (Figure 5). The sintering of a polycrystalline phase is significantly more energetically difficult than the amorphous phase, which suggests that it is favorable for amorphous materials to obtain full density before any significant crystallization.¹¹ However, experimental results show that sintering and devitrification of amorphous silica will occur concurrently, making it more complicated to deconvolute the processes.¹⁶⁻¹⁹

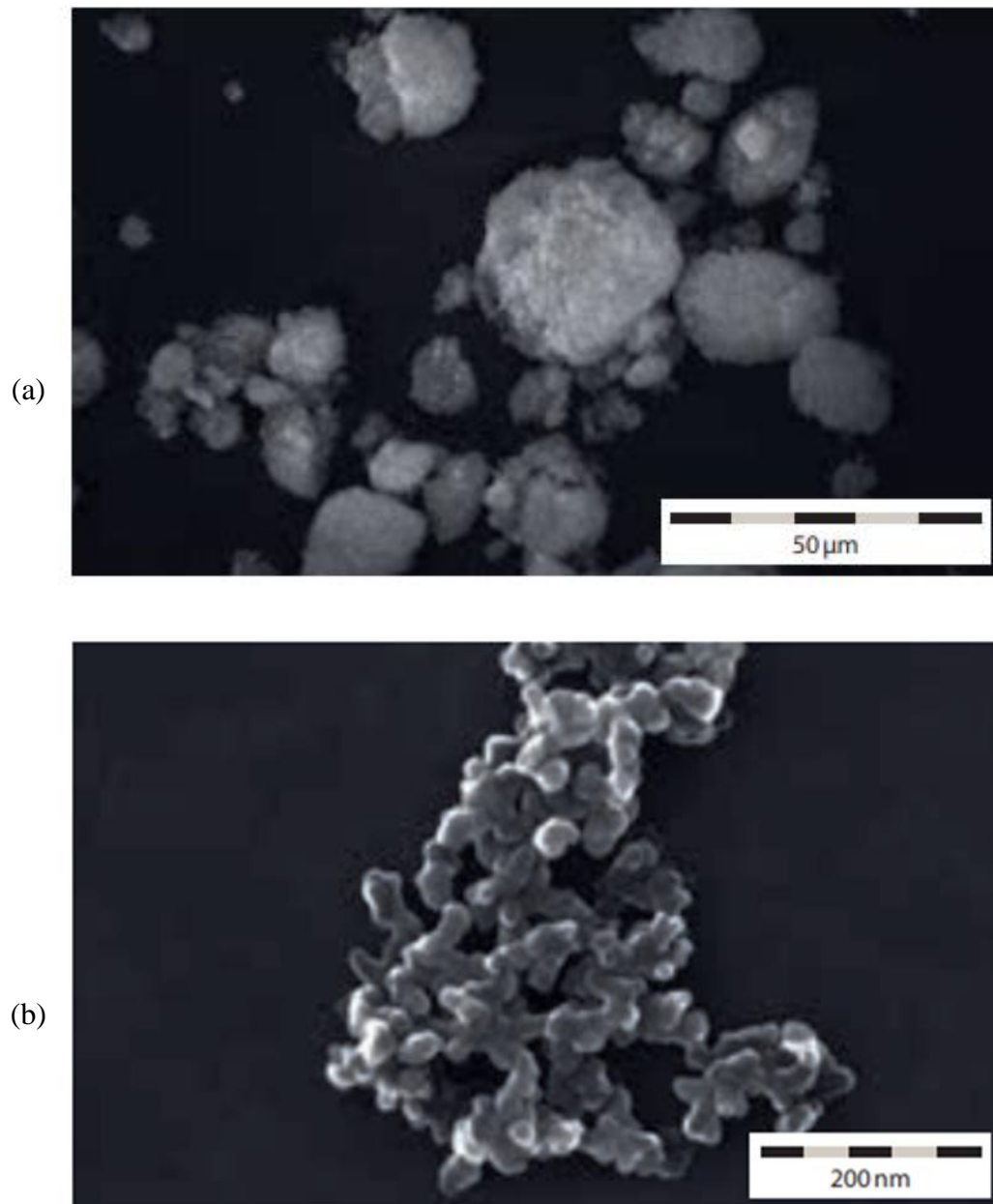


Figure 1: SEM images of Aerosil fumed silica. (a) Example of an agglomerate particle (b) example of an aggregate separated from the agglomerate by vibrational dispersion, clearly showing primary particles that have merged and cannot be separated.

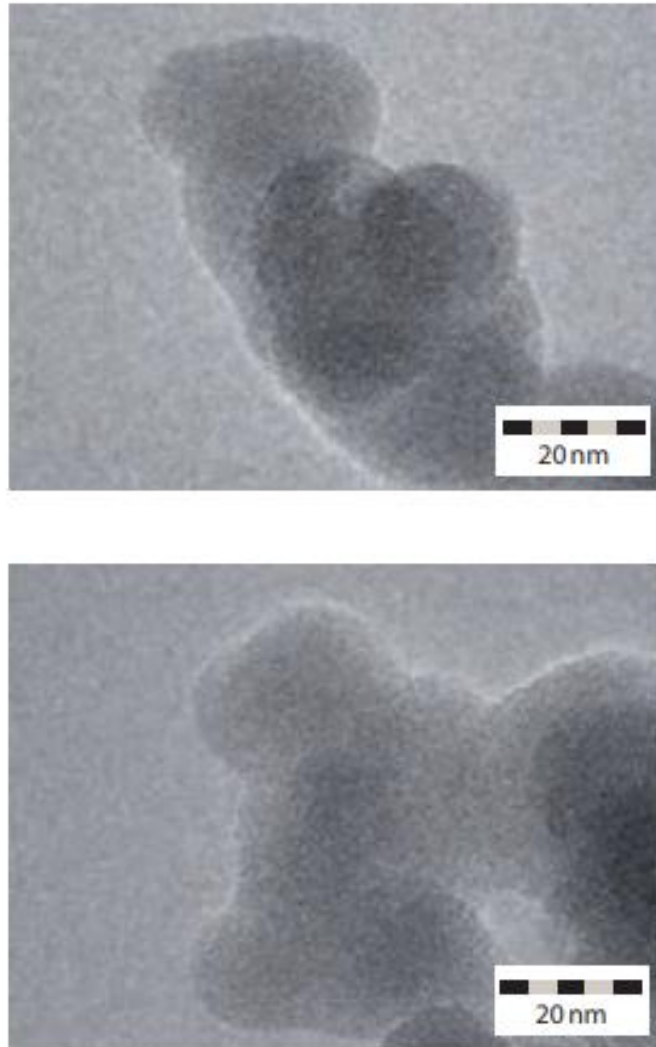


Figure 2: HRTEM images of Aerosil fumed silica aggregate particles, focusing on the merging zones of the primary structures. Merging can occur by impact following pyrolysis or facilitated by reactions with hydroxyl groups.

D. Silica Crystallization Kinetics

A multitude polymorphic crystalline phases of silica are known to exist, but most are metastable, and several require extreme geothermal conditions to form. A phase diagram, after V. Swamy et al.²⁰, is given for reference (Figure 3). While α -quartz is the only stable polymorph at normal environmental temperature and pressure (and is the predominant naturally occurring phase of silica in the earth's crust), tridymite and cristobalite are known to be transient, and also persist as metastable phases. Quartz is significantly more dense than the other forms, and rearrangement of silica tetrahedra requires the breaking and reforming of strong bridging oxygen bonds. Cristobalite tends to be the first devitrification product even when sufficient thermal energy is supplied for the other phases, simply because it is a less energy-intensive transformation.²¹ According to Ostwald's step rule, the material will then undergo further phase transformation as permitted energetically.

Geological samples of tridymite and cristobalite are known to have been formed during devitrification of volcanic ejecta which are quenched rapidly in air.²² Slow devitrification of volcanic glass also produces cristobalite, samples of which are colloquially known as "snowflake obsidian."

Under non-extreme conditions, devitrification of silica typically produces β -cristobalite via a heterogeneous nucleation from surface defects or impurities. Crystallization has been shown to occur at 1100 °C and higher temperatures. Upon cooling through ~250 °C, cubic β -cristobalite undergoes a displacive phase transformation to form tetragonal α -cristobalite, the low temperature polymorph. Figure 4 shows molecular schematics the high and low temperature forms of cristobalite. The phase transformation also results in extreme changes in thermal expansion; spontaneous strains of -1% and -2.2% along the a- and c-axes, respectively. The overall volume change (of ~4.5%) more often than not results in dramatic fracture. Ceramic artists are notoriously wary of cristobalite inversion in their wares for this reason.

Time-temperature-transformation (TTT) diagrams for devitrification of silica have been experimentally derived in several cases.^{11,16} A schematic is given in Figure 5; the onset of

crystallization at 1150 °C is typically on the order of hours, or at a higher temperature of 1550 °C occurs more rapidly. It should be noted that the presence of -OH groups and/or impurities facilitates crystal nucleation, and devitrification is thus affected by the thermal and processing history of the material and also the environmental conditions (e.g. humidity) under which devitrification is observed.

As a devitrification product, cristobalite often grows preferentially along the (101) crystallographic direction, hypothetically as a result of the lower energy requirement for crystal growth in this direction.²³ This is also perhaps facilitated by the anisotropy of the glass structure and the fact that minimal reorganization of silica tetrahedra are required for the phase transformation from glass to cristobalite.^{21,23}

Despite its regular occurrence, the transformation of amorphous silica to cristobalite is still not well defined, and quantitative analysis is difficult due to the sensitivity of the system to the presence of water or impurities.^{12,24} Again, the reactivity of the surface of amorphous silica is highly dependent on the quantity and location of hydroxyl groups, which is affected by how the material was processed, stored, and any other treatment it may have received.

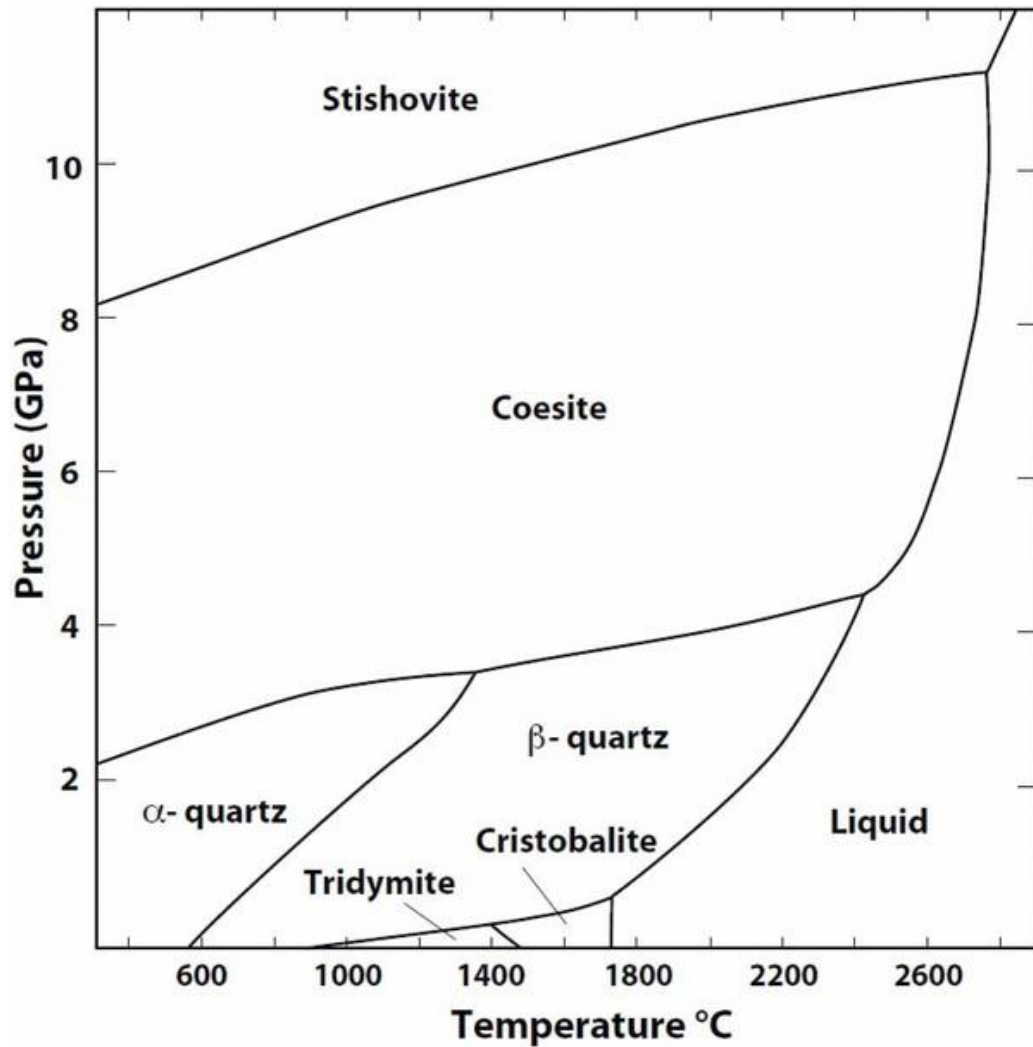


Figure 3: Silica phase diagram. While quartz is the only stable polymorph of SiO₂, it is most energy intensive to form. Therefore, non-equilibrium phases (glass, tridymite, cristobalite, etc.) which are metastable often persist.

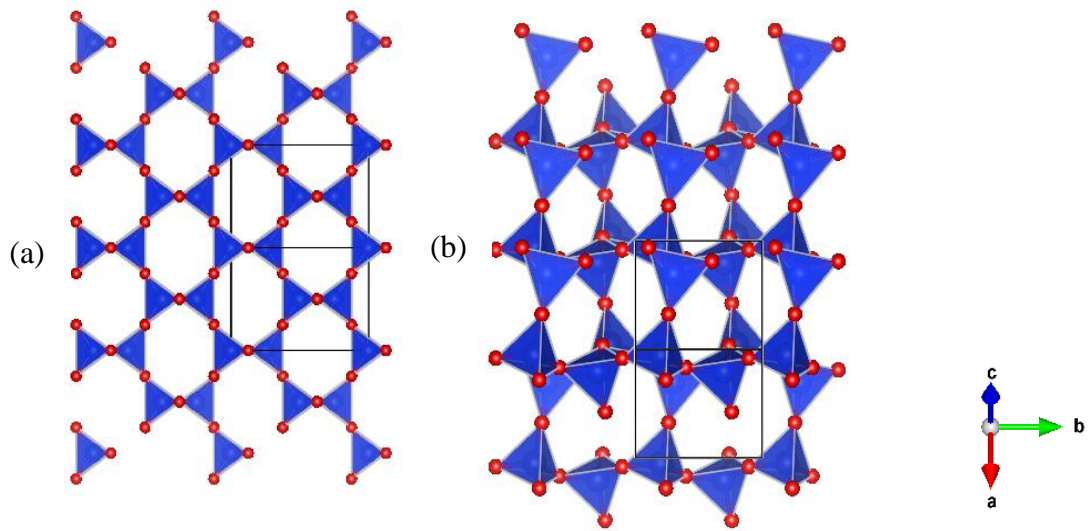


Figure 4: The high and low temperature forms of cristobalite. (a) β -cristobalite, a cubic phase stable above 250 °C transforms to (b) tetragonal α -cristobalite on cooling via a displacive, random tilting of silica tetrahedra.

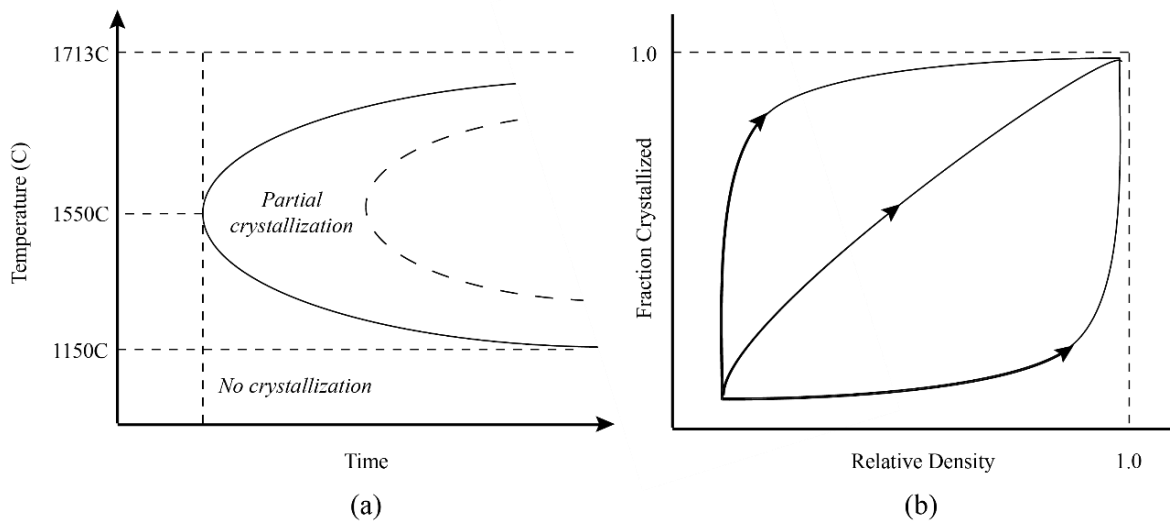


Figure 5: General schematics of (a) Time-temperature-transformation (TTT) diagram for crystallization of amorphous silica, and (b) pathways for devitrification and densification during sintering.

E. Pulsed Electric Current Sintering

The processing method explored in this work, referred to as “Pulsed Electric Current Sintering”, is a sintering technique utilizing an axial pressing force and pulsed direct electrical current under low atmospheric pressure, typically a vacuum. The current passes directly through a graphite die containing the sample, resulting in joule heating of the die ensemble. If the powder itself is electrically conductive, this local heating will also occur in the sample itself, as the current and thus resistive heating power is distributed along a percolative pathway via contact points between particles. In contrast to hot pressing, in which heat is provided by external elements, resistive heating allows for incredibly fast heating rates, reportedly as high as 1000 °C/min.²⁵

Achieving high density samples at lower temperatures and/or shorter processing times is practically and economically beneficial. In addition to being more energy efficient, PECS has been shown to reduce volatilization and undesirable phase transformations, and to suppress grain growth in metals and polycrystalline ceramics. With calibration and accurate monitoring of the internal temperature, it is possible to obtain valid axial shrinkage data. The ability to monitor reactions in situ via minute, transient temperature fluctuations and/or changes in chamber pressure has also been preliminarily demonstrated.²⁶

Several excellent reviews of the PECS method and its history exist,²⁷⁻³⁰ but while much evidence demonstrates the superiority of PECS to traditional sintering methods in certain cases, there is very little robust scientific explanation of the observed advantages (fast densification, desirable microstructure, etc.). Despite this, PECS has evolved from an exotic experiment to a viable processing route, gaining popularity in multiple disciplines ranging from metal fabrication to optics and even biomaterials.

The basic experimental set up is shown schematically in Figure 6. The sample, typically a fine powder, is loaded in the center of a graphite die, which is placed between an upper and lower punch. These punches can apply a compressive force to the die and powder, and they also act as electrodes for current to be sent through the ensemble.

F. On the Presence of Plasma

PECS is colloquially referred to as “Spark Plasma Sintering”. The origin of the name harkens back to the original inventor of the technique, who theorized that the favorable sintering results he obtained resulted from plasma generation induced by the applied current and coordinating electric field. The existence of this so-called electrical spark discharge phenomenon has been continuously debated, and no unambiguous evidence supporting it has been presented to date.²⁸⁻³⁰ It has been tentatively accepted that hot spots at the points of contact between conductive particles may be extreme enough to locally melt and vaporize the material, resulting in enhanced neck formation and growth from the activation of additional mass transport mechanisms. When considering quintessential electrically insulating materials, such as alumina or silica, no current is expected to pass through the sample and thus the generation of spark discharge can be ruled out.³¹⁻³⁴ Figure 7 (after Guillon et al., Anselmi-Tamburini et al., and Wang et al.^{28,35,36}) demonstrates this with a schematic comparison of the current flow through the die ensemble for an electrically conductive and insulating sample, based on a computational study. In this document, the term “Spark Plasma Sintering” is avoided in order to avoid confusion associated with and propagation of invalid assumptions about the technique.

G. Known Issues and Challenges

There are several things of import to note regarding the experimental set-up. First, temperature is typically measured by an optical pyrometer focused on the external surface of the die. The actual temperature of the sample tends to be higher than the die wall for insulating materials, but lower for electrically conductive samples.^{28,37} This is important, because the heating program (i.e. the current through the sample) is controlled by the temperature measured by the pyrometer.

Thermal gradients are present through the die ensemble which alter the sintering behavior of the sample.³⁸ The discrepancy between the inner and outer temperatures can be significant. The gradients are dependent on many things, including the geometry of the graphite die and spacer parts, the thermal diffusivity and electrical conductivity of the

sample,³⁹ and also the characteristics of the current provided by the equipment.^{35,40} Figure 7 compares the calculated equilibrium temperature distribution within the die ensemble for an electrically conducting and insulating sample, showing a persistent difference that increases in magnitude to ~150 °C at higher temperatures. Application of fast heating rates also influences the equilibration of the temperature within the die. It has been estimated that this can take about 100 seconds,³⁹ which is a substantial increment when the entire process (pressing, heating, cooling) only spans minutes.

Experimental parameters employed tend to be poorly recorded in publications, and different PECS machines operating under supposedly analogous parameters tend to produce different results.^{28,41} Most users working with PECS can collect consistent data from a single machine using the same measurement method.

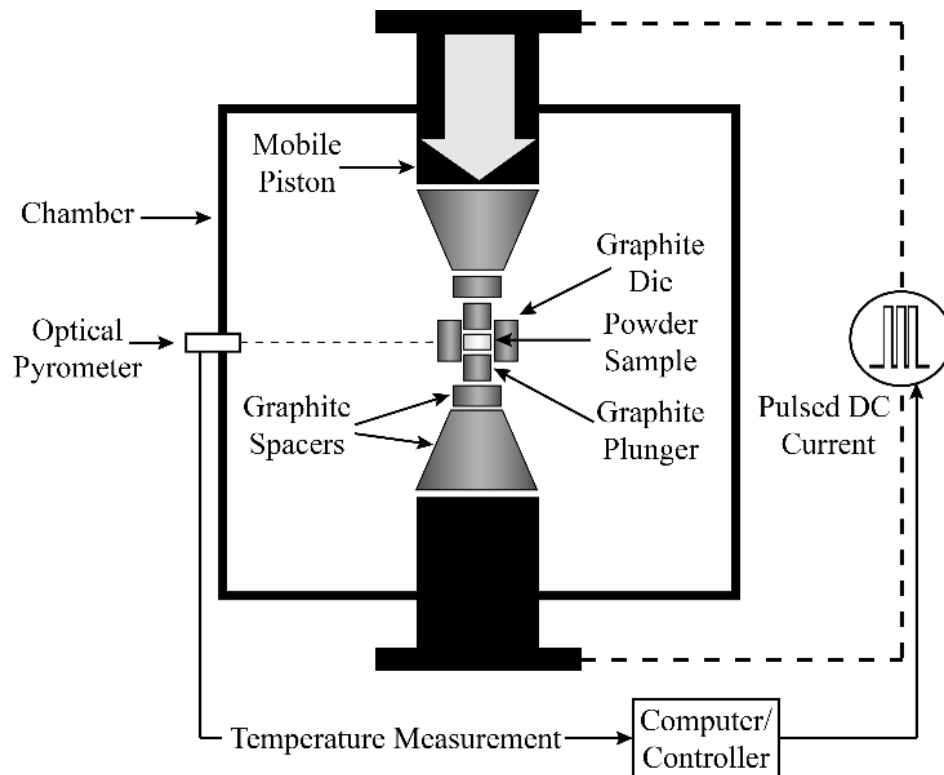


Figure 6: Experimental set-up for PECS processing.

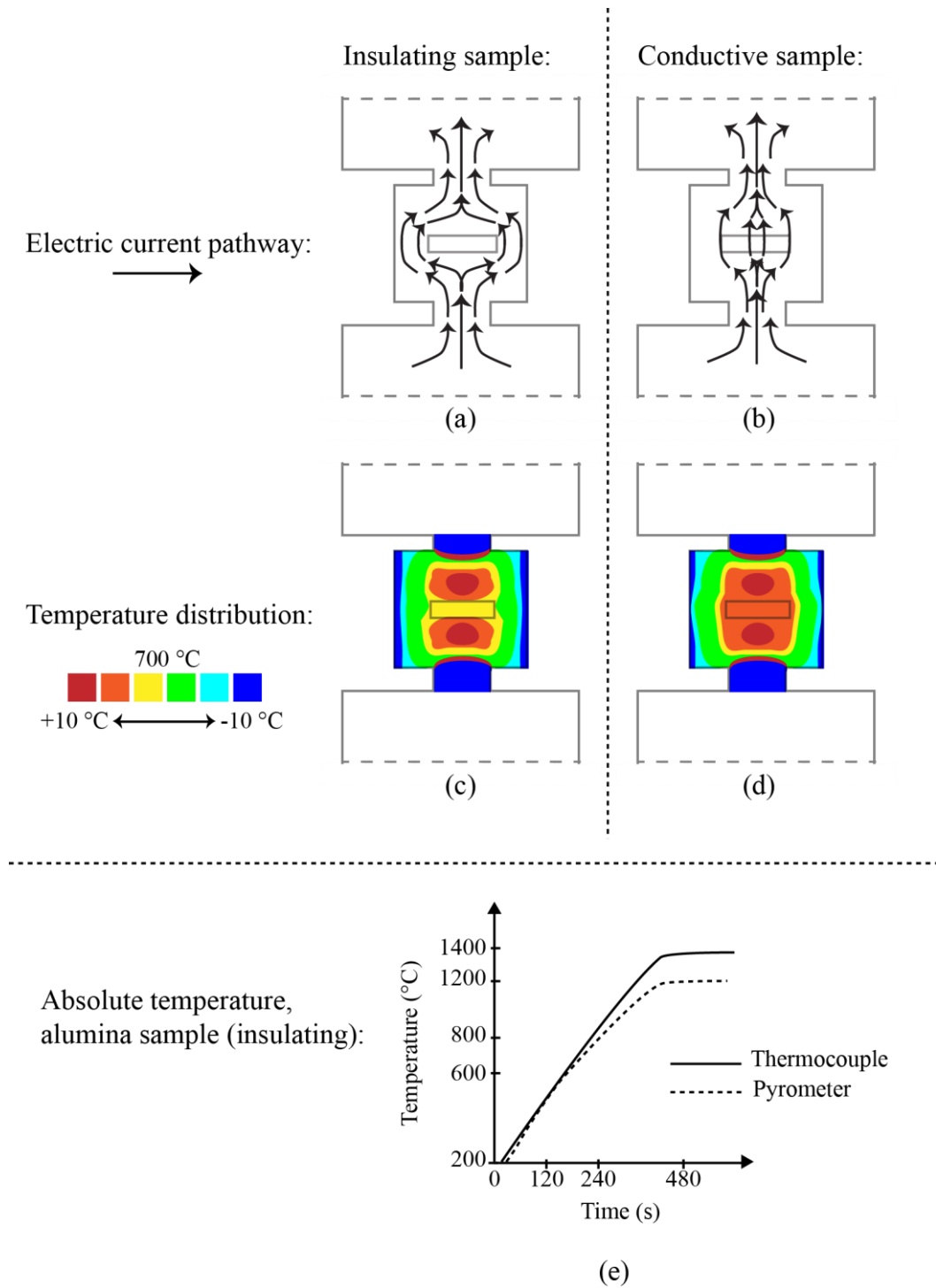


Figure 7: Comparisons of current density and temperature variation through the die ensemble for electrically insulating and conducting samples. (e) Shows the different temperatures measured by optical pyrometer and a thermocouple inserted into the die wall of the same sample of an insulating material. Adapted from Guillon et al., Anselmi-Tamburini et al., and Wang et al.^{28,35,36}

III. LITERATURE REVIEW

There are several published studies in which pulsed electric current sintering of silica and silicate glasses has been preliminarily explored and proven to be feasible.

In 2002, Koide et al.⁴² fabricated dense silica glass from 70 μm quartz particles heated to 1773-1873 K via PECS. It was noted that samples heated at a faster rate (100 $^{\circ}\text{C}/\text{min}$ vs 50 $^{\circ}\text{C}/\text{min}$) tended to crystallize on the surfaces. Devitrification was associated with insufficient time to equilibrate stresses resulting from thermal gradients in the sample. Koide et al. also showed that the properties of silica glass processed in this way were the same as traditional fused silica, with some evidence present in the UV-absorbance spectra of oxygen deficiency defects from reducing atmosphere.

A 2008 paper from Mayerhofer et al.⁴³ reported sintering of silicic acid nanoparticles at 1273 K. Loss of transparency of fully consolidated silica glass samples was identified as being due to a high concentration of residual -OH groups. Nuclear Magnetic Resonance results suggested that short and medium range order was the same as traditional fused silica, but Raman spectra identify fewer 3-4 membered rings than expected.

A series of studies were carried out by Barazani, Torikai, et al. from 2011-2016 utilizing α -quartz and amorphous silica powders with varying particle size over a wide range of sintering temperature (1225-1350 $^{\circ}\text{C}$) and heating rates.^{26,44,45} They reported that transparent silica free from bubbles was obtained for slow heating rates, and that samples processed with higher heating rates required higher final temperature to achieve full consolidation. They were also able to fabricate composite samples of silica glass reinforced with α -quartz crystal. Barazani et al. also observed gas release from sample at various temperatures, and concluded that fast heating rates can lead to gases being trapped within the sample. Bubble formation can be minimized by slow heating rates during a temperature range after gas release but before rapid consolidation, and by holding at high temperature to allow gases to diffuse out of the sample. Regions of non-transparent glass within the samples indicated thermal gradients, where the plungers act as primary heat sources and the die wall tends to dissipate heat.

Zhang, Tu, and Goto⁴⁶ published in 2012 a comparison of PECS and pressure-less sintering amorphous silica powder, and found the PECS samples to be more transparent. They observed no crystallization of the PECS fused silica below 1673 K, but the sample sintered traditionally did devitrify.

Zhang et al.⁴⁷ and Shi et al.⁴⁸ sintered a commonly synthesized sol-gel derived mesoporous silica, SBA-15, in two related studies published in 2015 and 2016, respectively. They observed rapid densification during a narrow temperature window of 1203-1253 K. Sinterability seemed to be enhanced by the presence of mesopores in the starting glass powder, perhaps due to increased surface area. The mesoporous microstructure of the starting powder collapsed completely during sintering. They observed evidence of a radial temperature gradient existing with higher temperature in the center of the sample than the edges, affecting homogeneity. Devitrification was observed and the crystalline phase identified as cristobalite.

Dibandajo et al.⁴⁹ and Maheshwari et al.⁵⁰ sintered SBA-15 mesoporous silica to create compacts with bi-modal meso-macroporous microstructure. It was again observed that the mesoporosity of the SBA-15 powder was maintained until samples were heated above 850 °C, at which point the mesopores collapsed. Contrary to the results of Zhang et al. and Shi et al., the mesopore channels characteristic of SBA-15 were retained during PECS under certain conditions, only collapsing at high sintering temperatures (>950 °C). It was found that the physical-mechanical properties could be correlated with the degree of macroporosity, surface area, and pore morphology of the samples.

Röding, et al.⁵¹ studied the microstructure of silica glass sintered by PECS. A selective etching process was used to reveal a microstructure with distinct “granule” boundaries correlating to the surfaces of the particles before sintering. They were also able to etch a 3-dimensional pore system at the boundaries. A simple model based on sintering of spherical particles was found to successfully predict the microstructure of the glass.

The varied scope and findings of these works imply that the processing variables employed are of critical importance in obtaining consistent and predictable results. These include origin, phase, particle size, processing history, etc. of the starting raw silica material,

heating rate, die diameter, axial compression, and post-processing. Additionally, employing fast heating rates can result in gas release from the sample that is violent enough to fracture the die. In light of these considerations, a methodical approach must be applied to the production of quality glass samples via PECS. Amorphous silica is a natural starting point for investigation because of its simple composition, usefulness in a wide range of applications, and historically well-characterized structure and properties. The knowledge gathered from this system can then be applied to fabrication of glasses that are difficult to produce by traditional melting techniques, or to the creation of glass-ceramic composite materials by PECS.

IV. EXPERIMENTAL PROCEDURE

Approximately 1 g samples of Aerosil OX50 powder (Evonik Industries) were loaded into 0.75 in. internal diameter graphite dies (AR-14, Ohio Carbon Blank) lined with thin graphite foil paper (2010-A, CeraMaterials), and manually pressed to 1000 psi before being placed into the PECS chamber (FAST/SPS sintering equipment from FCS Systeme, GmbH). Aerosil OX50 is a high purity fumed silica with a low specific surface area and high tamped density, the properties of which are tabulated below (Table 1). Note that weight loss on drying is a widely used test method to determine the moisture content of a sample, although occasionally it may refer to the loss of any volatile matter from the sample. Loss on drying does not usually refer to chemically bound water. Aerosil OX 50 is untreated, resulting in a hydrophilic surface. This means that after extended storage, the glass will adsorb water from the air until it reaches an equilibrium state of hydration. The presence of water is obvious from the IR spectrum of the starting powder (Figure 8).

The basic experimental set-up is shown schematically in Figure 6. The powder sample is held inside of a graphite die, which is placed between an upper and lower punch. These punches apply a compressive force to the die and powder, and they also act as electrodes for current to be sent through the ensemble. Considering the previously discussed variables, it should be noted that the powder sample was placed in the exact center of the PECS column and care taken to align the die punches and other graphite spacers consistently to avoid introduction of avoidable experimental error.

The samples were then sintered in vacuum according to Figure 9 and the parameter matrix portrayed in Table 2. Pressing force was increased first, and then temperature ramped to the set point. It is important to note that temperature is measured by an external optical pyrometer (see Figure 6) and does not reflect the temperature experienced by the powder sample contained within the die, but rather at the die surface. After hold time, both axial pressure and temperature were relieved simultaneously. A heating rate of 150 °C/min with no hold at the maximum set point was employed for each temperature set point, and then additional heating rates and hold duration were explored at 800 °C and 1100 °C.

After sintering, samples were removed from the dies and the graphoil was peeled off, and then the sintered compacts were heat treated at 900 °C for 5-10 hours under flowing oxygen to remove residual graphite from the pellet surfaces.

Samples were sectioned and prepared for characterization as necessary. Fracture surfaces of some samples were etched in 20% KOH at 60 C or 17% HF at room temperature to enhance features of the microstructure before imaging. Some samples were coated with gold-palladium prior to scanning electron microscope (SEM) imaging to reduce charging of the surface. Powdered samples were degassed at 150 °C under flowing N₂ (Micromeritics FlowPrep™ 060) for at least 2 hours before He-pycnometry (Micromeritics AccuPyc II 1340) and Brunauer-Emmet-Teller (BET) gas adsorption testing (Micromeritics TriStar II). Fourier-transform infrared (FTIR)-resonance spectra (Nicolet™, Thermo Electron Corp.) reported are an average of 200 scans at 8 cm⁻¹ resolution.

Diffraction data were collected in Bragg-Brentano geometry using a Bruker D8 Advance equipped with Cu K α radiation and a position sensitive detector. Samples for phase identification were prepared by manual grinding and loaded onto an off-axis quartz plate (i.e. zero-background holder). Meanwhile, internal fracture surfaces created by the thermal expansion mismatch between the crystallized and vitreous sample regions were oriented in malleable mounting putty as illustrated schematically in Figure 39.

The powder diffraction line profile of the crystallized cristobalite was noted to have features indicative of 1-D layer disorder.⁵² This was investigated using powder pattern simulations computed by the well-established code DIFFaX⁵³. A layer definition, based on β -Cristobalite, coupled with a transition matrix (corresponding to the estimated frequency of stacking faults) was used to calculate diffraction patterns.

A. Considerations Regarding Silica Volatilization in Reducing Conditions and Reactions Between SiO₂ and Graphite

As previously noted, SiO₂ powder is contained within a graphite die during PECS, so it is prudent to consider equilibria in the Si-C-O system. A sample in the PECS chamber experiences reducing conditions. Ramond et al.⁵⁴ noted a coloration in spark plasma sintered glass samples that was associated with carbon contamination. Reactions at the interface between silica and graphite, and/or diffusion of carbon into the glass could facilitate heterogeneous nucleation of cristobalite.

Solid state reactions in the Si-C-O system have been shown to have intermediate gaseous byproducts per the following equations:



At temperature less than 1400 °C the dominant mechanism for carbon-rich materials first involves a solid-state reaction of SiO₂ and C leading to SiC formation and removal of CO (Equations 1, 2). When the system is depleted of its free carbon however, another reaction can also proceed parallel to the former one, where SiO₂ and SiC react leading to a loss of gaseous SiO and CO (Equation 8).

In the experimental set-up for PECS, the chamber is kept under vacuum during processing. Therefore, it can be assumed that much of the gas phases are removed from the system before the secondary reaction(s) can proceed. Despite this, it would be expected that silicon carbide would be produced at the silica-graphite interface, which would then proceed to

volatilize silicon-oxygen bonds at the sample surfaces, releasing the gaseous products. It should also be noted that these reactions are kinetically limited, as they occur at the interface of the silica sample and the graphite die.

Table I: Properties of Aerosil OX50.

| Parameter | Value |
|---|--------------|
| Density [g/cm ³] | 2.28 |
| | *2.30 ± 0.02 |
| Specific surface area (BET) [m ² /g] | 35-65 |
| | *42.8 ± 0.4 |
| ⁺ Loss on drying [wt%] | ≤1.5 |
| Approximate tamped density [g/L] | 100 |

**marks experimental measurement, all other values reported by manufacturer¹*

⁺See text. Fumed silica powder is hydrophilic and will adsorb water from the air.

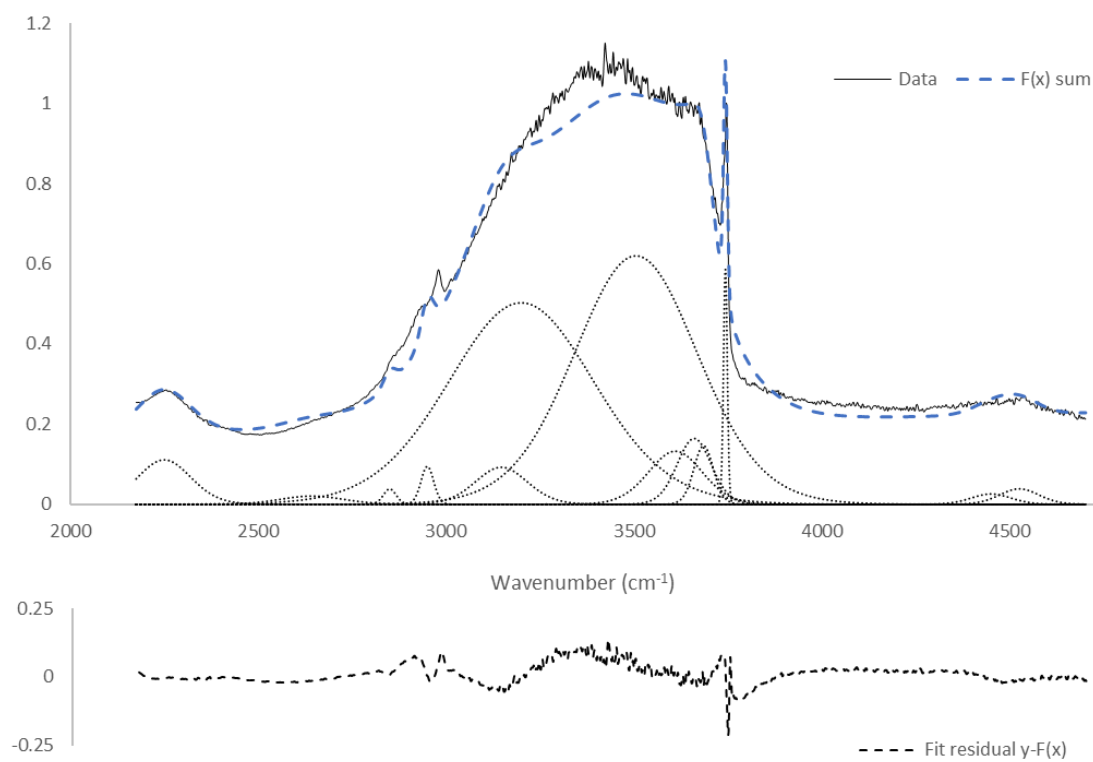


Figure 8: Fitted FTIR Spectrum for Aerosil OX 50 (aged/hydrated). Band assignments are given in Table 2.

Table II: FTIR Absorbance Band and Sub-band Assignments

| <i>cm⁻¹</i> | <i>Structural Element</i> |
|------------------------|---|
| 3685 | Sub-band: -OH stretch hydrogen bonded silanol-H ₂ O in type I silica |
| 3660 | Sub-band: -OH stretch hydrogen bonded silanol-H ₂ O in type II silica |
| 3610 | Sub-band: -OH stretch hydrogen bonded silanol-H ₂ O in type III silica |
| 3505 | Sub-band: -OH stretch hydrogen bonded silanol groups |
| 3850 | Sub-band: combination torsion and stretching of SiOH groups |
| 4525 | Asymmetric and symmetric combination bending and stretching of silanol group |
| 4450 | |
| 3745 | "Free" -OH groups |
| 2478 | -OD stretch hydrogen bonded silanol groups |
| 3200 | Combination bending and stretching of -OD group |
| 2645 | "Free" -OD groups |
| 2250 | -SiH stretching mode |
| 2950 | -CH |
| 2850 | |

**where D is for deuterium; these bands were calculated from the known -OH bands by accounting for the 2:1 mass ratio of the ions. The natural occurrence of deuterium is 1 atom in every 6420 of hydrogen. These bands are included because (1) the Aerosil product information manual indicated they may be observed, and (2) they improve the overall fit.*

Table III: Experimental Parameters.

| Parameter | Value | | |
|--|-------------------------|---------------------------------------|--------------------|
| | I. | II. | III. |
| Pressing force [kN] | 5 | 5 | 10, 15, 20, 25, 30 |
| Heating Rate [$^{\circ}\text{C}/\text{min}$] | 150* | 50, 100, 150*, 200 | 150 |
| Max. Temp. [$^{\circ}\text{C}$] ⁺ | 500, 600, 700, 800, 900 | 920, 940, 960, 980, 1000, 1100, 1200, | 1100 |
| Hold time at max. temp. [min] | 0*, 1, 5, 10 | 0*, 1, 5, 10 | 0 |
| Cooling Rate [$^{\circ}\text{C}/\text{min}$] | 100 | 100 | 100 |

⁺*as measured by external pyrometer*

**this combination of heating rate and hold time was employed for all temperature set points*

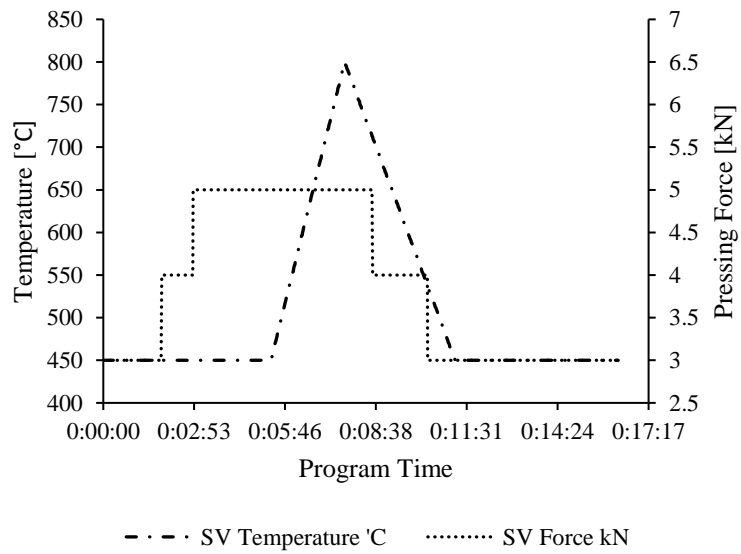


Figure 9: Example PECS program to sinter a sample at 800 °C with 5 kN of pressing force, with a heating rate of 100 °/min.

V. RESULTS AND DISCUSSION

The results of this study will be reported and discussed in several distinct parts. To begin, observations regarding the inherent variability of PECS and reproducibility of results will be discussed in such a way as to frame the specific outcome of the experiments described in the previous section. The specific results will then be organized as follows:

First, sintering at low temperatures (sub- T_g) was found to produce compacts with a continuous porous microstructure. Evidence of graded porosity was observed across the samples resulting from thermal gradients present within the sintering apparatus.

Next, dense, transparent glass compacts were formed via consolidation above the softening point of the glass. The nominally dense glass parts produced this way contained macroscopic defects, such as trapped bubbles, and were prone to devitrification at the corners and surface. No correlation was found between processing parameters and the presence or extent of these flaws, implying an inherent inconsistency of applying PECS to fabrication of silica glass parts, especially at higher temperatures.

The third section is comprised of a short treatise on the effect of axial pressing force applied during sintering is presented. It is demonstrated that increasing the pressing force drives down the observed onset of viscous sintering of the glass as additional mass transport mechanisms are activated. Pores/bubbles are rapidly removed from the glass at a temperature well below that which is necessary to obtain similar results when no axial force is applied. Devitrification also seemed to be suppressed by increasing the pressing force. Both of these observed effects result from the disruption of thermal gradients as the glass is encouraged to flow from where it is least viscous into the cooler center of the sample.

Finally, the rapid devitrification of silica observed to occur during PECS is investigated and elaborated upon. Crystallization occurs earlier and much more quickly than would be expected during traditional pressure-less sintering, and the resulting phase shows a unique, cross-hatched microstructural texture. The crystalline phase was identified as α -cristobalite exhibiting preferential growth normal to the $\langle 101 \rangle$ crystallographic planes. The presence of obvious shoulders in some diffraction peaks indicated the presence of

stacking disorder in the precipitated α -cristobalite, and studies of the (011) diffraction line profile indicated the presence of twin boundaries with a 5% probability along the 111 (trigonal) axis of β -cristobalite. Twin boundary stacking faults in cristobalite are commonly observed in naturally occurring crystals, as they are inherently created when transitioning from the high (β) to low (α) temperature polymorph of the phase.

A. Inherent Variability of Results According to the Experimental Set-up

There are several things of import to note regarding the experimental set-up. First, temperature was measured by an optical pyrometer focused on the external surface of the die. Thus, the temperature recorded by the machine is not the actual temperature experienced at the center of the sample. The actual temperature of the sample tends to be higher than the die for insulating materials, but lower for electrically conductive samples. It should also be noted that temperature will not equilibrate within the die ensemble until about 100 seconds of heating. Gradients exist, and these alter the sintering behavior of the sample. The powder must be suspended in the exact center of the PECS column to obtain reproducible results, so care need be taken to align the die, punches and other graphite spacers consistently.

Figure 10 shows vertical shrinkage during sintering as a function of temperature for multiple samples heated at a constant rate. At a given temperature, shrinkage varies by about 1%. This is not an alarming observation, but more worrisome is the fact that there appears to be an offset in the onset of different sintering regimes, indicating inconsistency of temperature measurement. This variability is estimated to be about ± 35 K. This increases the difficulty of comparing results by monitoring shrinkage rates during sintering, and makes error propagation even more important to consider when analyzing data quantitatively. So, assuming that the overall consolidation of the powder can be inferred from the piston position will clearly not yield reliable a conclusion.

Due to temperature gradients during sintering, the samples heated to between 900 and 1000 °C actually seem to have experienced temperatures both above and below the softening point of the glass. This incomplete consolidation results in dense glass and porous layers that can be observed in cross-sections of the samples (Figure 27). There was no correlation between the program temperature and the degree of consolidation of the samples (i.e. amount of fully fused, dense glass vs. porous center region). The presence of

“hot spots” during processing could be observed in some samples as locations where the glass surface layer is inconsistent (Figure 27 (c)).

Samples sintered above 1000 °C all underwent some degree of devitrification. It is generally accepted that the temperature must meet or exceed 1100 °C to activate crystallization, the thermal gradient which the samples experienced would appear to have been at least ~100 degrees across the 0.75 inch thick die wall.

All of this evidence points to an inability to correlate what the external pyrometer measures and the actual internal temperature at the center of the die ensemble, and the existence of extreme thermal gradients within the die ensemble. The combination of these actualities significantly lowered the chances for achieving reproducible results with this experimental set-up, despite adhering to the aforementioned precautions.

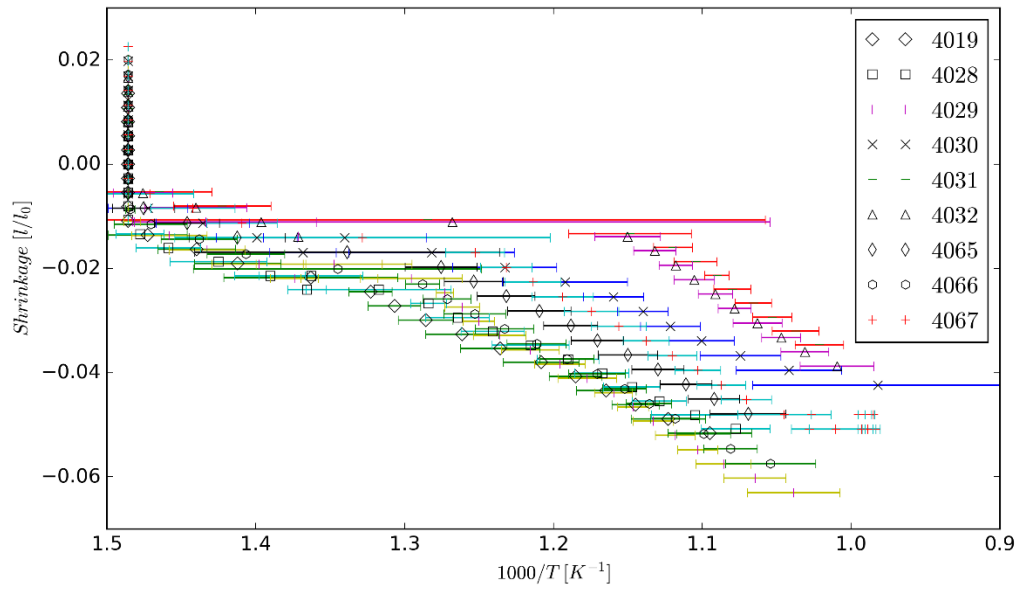


Figure 10: Variation in measured shrinkage with heating for samples heated to 800 °C at 100 °C/min. The onset of viscous sintering can be seen to be shifted by as much as 35 °C as measured by optical pyrometer at the exterior die wall.

B. Graded Porosity in Glass Scaffolds Fabricated via Pulsed Electric Current Sintering of Fumed Silica Nanoparticles at Temperatures ≤ 900 °C

Intermediately sintered, porous glass compacts were obtained via this processing route. Characteristic consolidation is shown in Figure 11, and Figure 12 is an optical micrograph of a typical sample. As expected, the porous silica samples allow transmittance of diffuse light. All samples remained fully amorphous and an open, meso-macroporous microstructure was confirmed by He-pycnometry, N₂ gas adsorption isotherm testing, and SEM.

Plotting piston position against temperature permits inference of sintering progress during the PECS cycle (Figure 13). It is clear to see that as samples are heated to higher temperatures a greater degree of sintering (as equated to permanent vertical piston displacement) is achieved. The relative piston position as reported by the instrument was corrected to reflect a zero displacement at the time the external pyrometer registers heating (i.e. above 400 °C).

At 600 °C and below, no significant permanent compression of the sample is observed, indicating that insufficient thermal energy was supplied to facilitate densification. This is also apparent in Figure 14 in which final piston position is plotted against temperature.

Skeletal density was determined by He-pycnometry, and was found to be ~ 2.30 g/cm³. The skeletal densities of the sintered and starting powders were equivalent, indicating the amorphous structure did not densify as a result of sintering. Further, the absence of entrained porosity, which would reduce the observed pycnometric density, implies only an intermediate stage of sintering has been achieved and a continuous, open pore network maintained.

FTIR spectra for the unprocessed Aerosil OX 50 silica powder, and a sample sintered at 800 °C are given in Figures 8 and 15, respectively. The absorbance bands as identified in

the figures are tabulated previously (Table 2). The approximate band widths and intensities were refined using the peak fitting program, *Fityk*⁵⁵. Note that these fits are qualitative, as the refined values do not take into account physical parameters related to the vibrational modes aside from the nominal peak positions. Quantum mechanical calculations would need be undertaken to improve this preliminary model.

It is clear to see that the starting powder is fully saturated with water and silanol groups. This is to be expected, as Aerosil OX 50 is an untreated fumed silica powder, and is thus hydrophilic. Of note is the sharp absorption band at about 3745 cm^{-1} , which is ascribed to “free” silanol groups. This refers to -OH groups on the surface of the silica particles/agglomerates. As the powder is heated and fused, this band grows while the others decrease as the sample dehydrates with applied heat and vacuum environment. The sintered glass has a continuous, open pore microstructure, and thus significant interior surface area which may be populated with surface -OH groups.

The gas adsorption testing showed a dramatic change between the starting powder and the sintered samples (Figures 18-19). The shape of the gas adsorption and desorption isotherms indicate uniform porosity, arising from regularly distributed spherical agglomerates or a network of pores with narrow mouths (ink-bottle pores) as is expected from the initial stages of sintering of silica. Pore size distributions were calculated from nitrogen gas adsorption/desorption isotherm data using the Dollimore-Heal method and analysis software from Micromeritics. Calculated surface areas were found to be very inconsistent, and no correlation was found between surface area measurements and changes in heating rate or holding time, despite slight changes in the isotherms that trend with temperature. There did seem to be a larger pore volume in samples sintered with faster heating rate, as would be expected, as the sample had less cumulative time at elevated temperatures (Figures 11-12). No correlation was found between cumulative pore volume measured by gas isotherm testing, and estimated porosity inferred from overall shrinkage of the compacts (Figures 13-14).

SEM imaging confirmed the continuously porous microstructure and revealed a distribution of pore concentration that trends with displacement along the vertical axis (pellet thickness). Figure 17 shows SEM micrographs of fracture surfaces near the edge

(a) and center (b) of the vertical cross-section of pellet. The image taken near to the sample edge shows the original particles to be deformed and fused together to create a nearly homogeneous microstructure, with little obvious porosity. In contrast, the image from the sample center portrays fairly uniform, spherical particles that have only just begun to form necks between them.

It is known that temperature gradients exist within the PECS die during sintering, and those have resulted in differing microstructures between the center and edges of the pellets. The outside surfaces are heated directly from the die punches, and then that heat must diffuse into the center of the sample. Thus, we see densified glass with few pores near to the exterior surfaces of the samples, but an open, porous microstructure at the centers (as demonstrated in Figure 17). The existence of a continuum of porosity across the samples is likely responsible for the inconsistency of the gas adsorption measurement results. The lack of effect of holding time on the pore distribution implies that the thermal gradient within the die ensemble does not equilibrate within 10 minutes, and as such may never do so. A higher heating rate would be expected to increase the magnitude of the thermal and thus microstructure gradient, but this was not confirmed with these experiments due to the additional contribution(s) to variability of the results.

To summarize, sintering at temperatures below the softening point of the glass results in intermediate sintering of the powder compact and in a continuous porous microstructure. The thermal gradient within the die results in gradated porosity, with enhanced densification/removal of pores at the outer surface of the compact. Hydrogen bonded water molecules were removed during PECS, but the concentration of silanol groups in the bulk glass remained relatively unchanged during sintering.

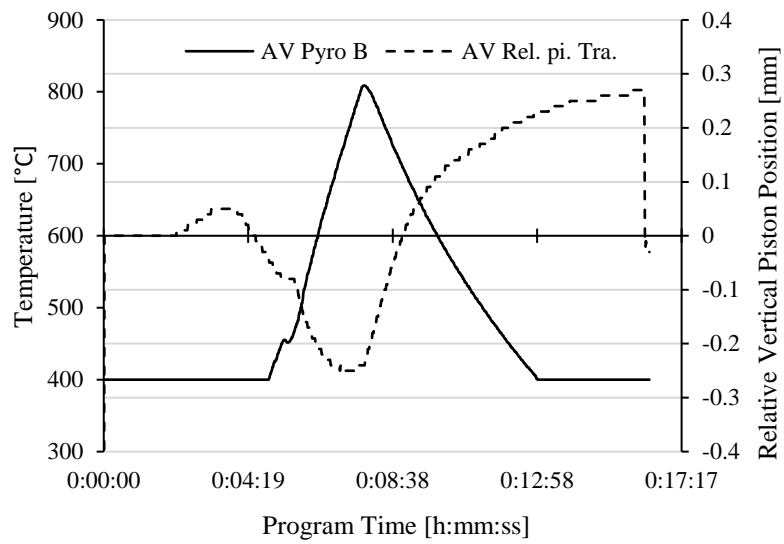


Figure 11: Sample PECS program output. AV Pyro B is the temperature as measured by external pyrometer, and AV Rel.pi.Tra gives the vertical displacement of the upper piston.

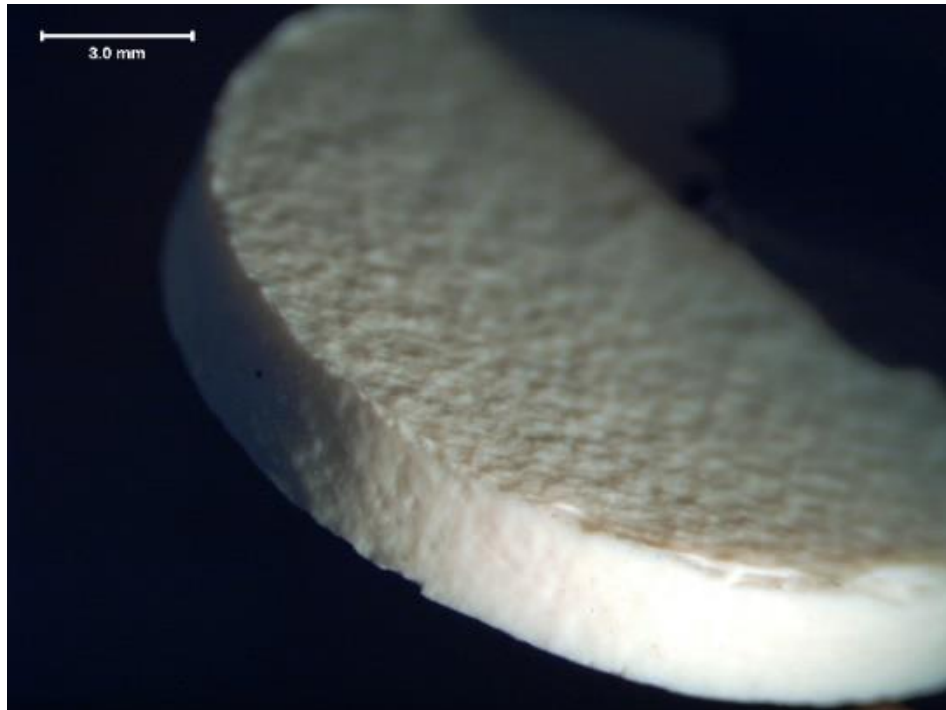


Figure 12: Optical micrograph of a typical intermediately sintered SiO_2 porous compact.

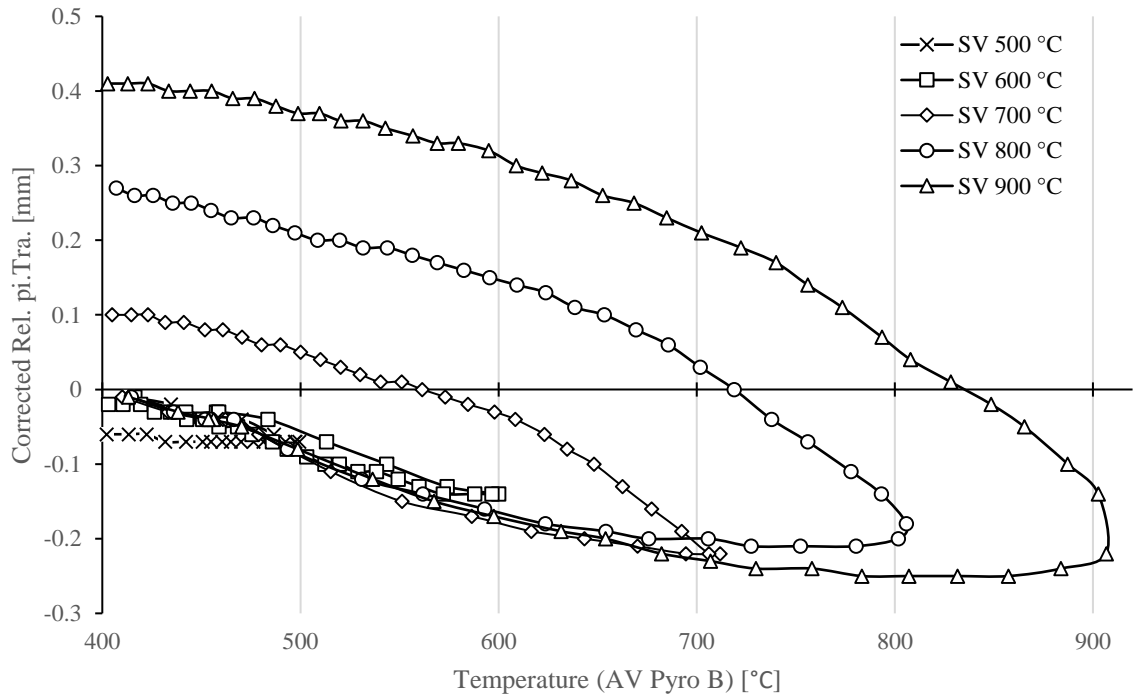


Figure 13: Characteristic consolidation visualized as piston position plotted against temperature. The initial (0 mm) and final piston positions relate to the degree of sintering achieved during heating and cooling. It should be noted that when cooling begins the pressing force is relieved simultaneously.

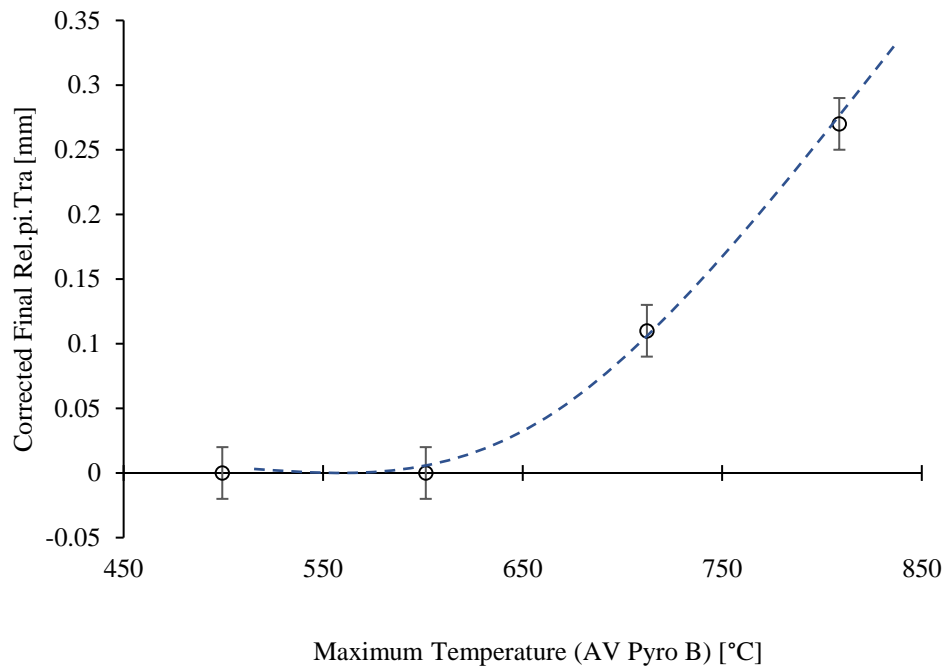


Figure 14: Final piston position (see Figure 15) vs maximum external die wall temperature. Dashed line provided as a guide to the eye.

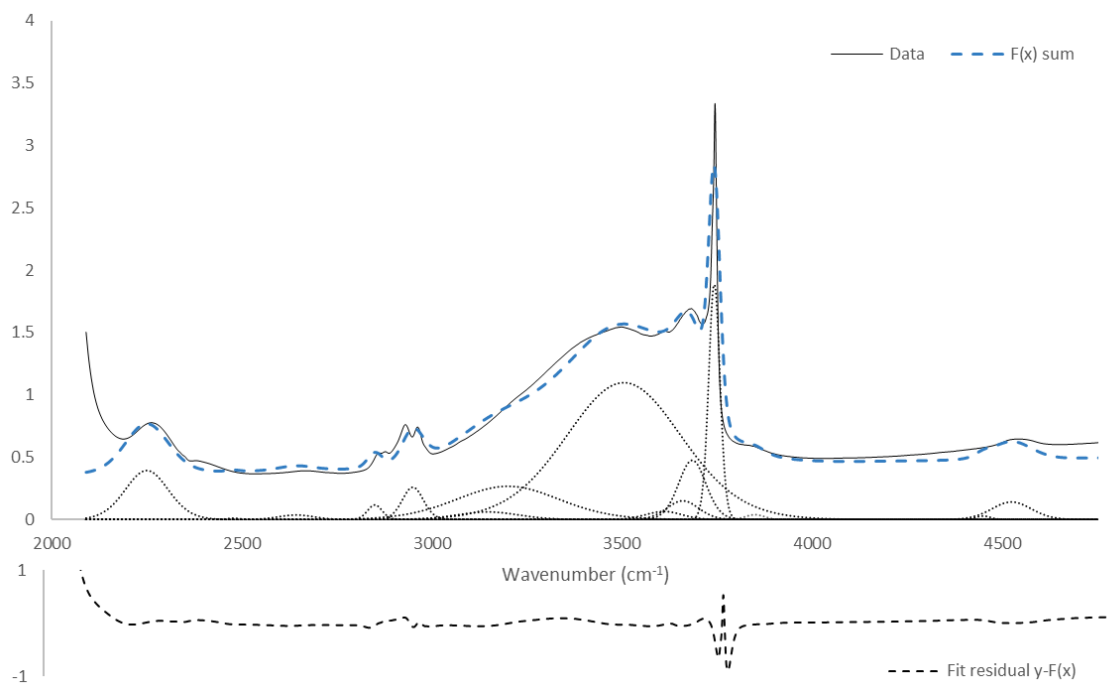


Figure 15: Fitted FTIR Spectrum for Aerosil sintered at 800 °C. Peak assignments are tabulated in Table 2. The spectrum for the un-sintered powder is given in Figure 8.

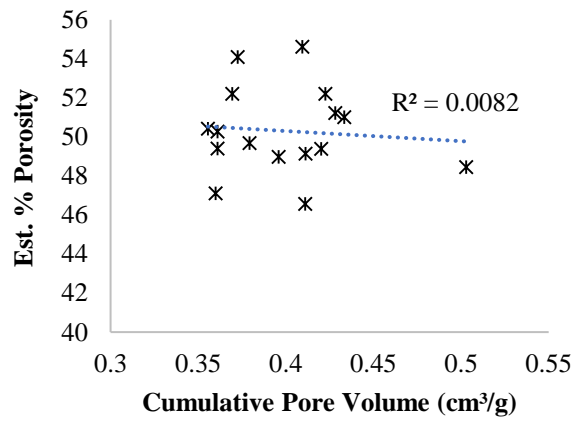
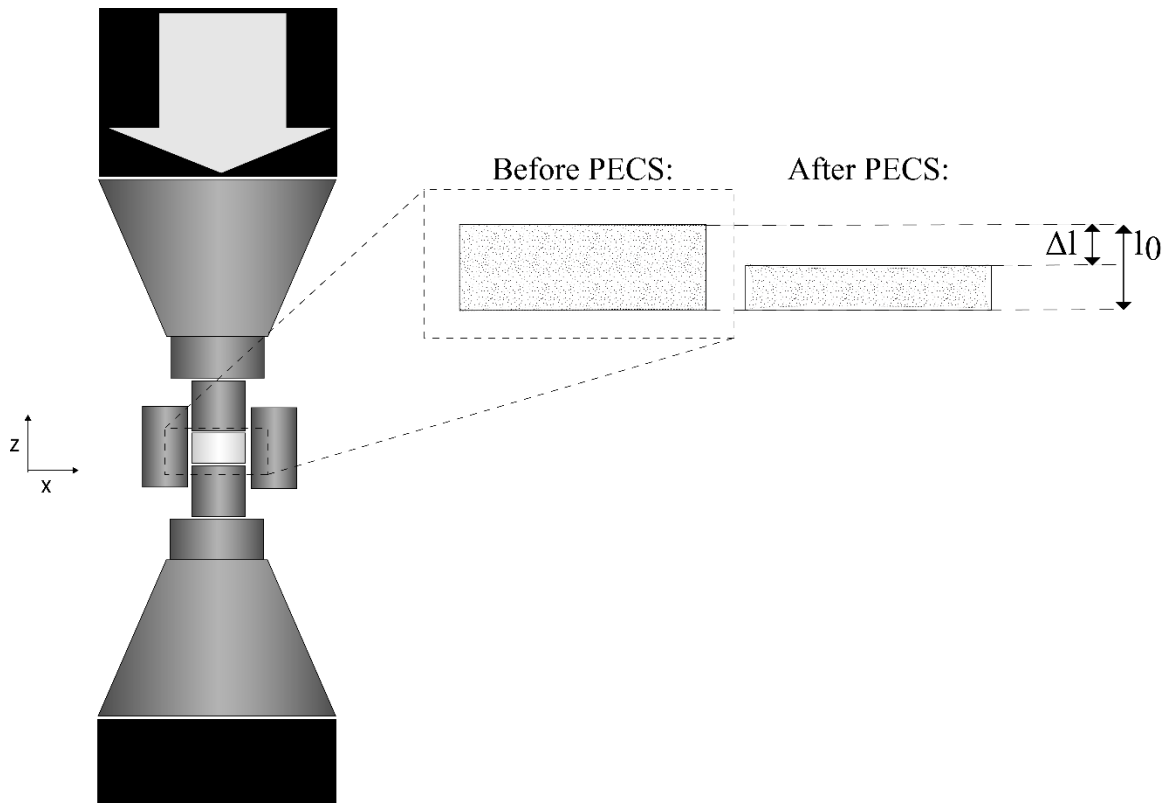
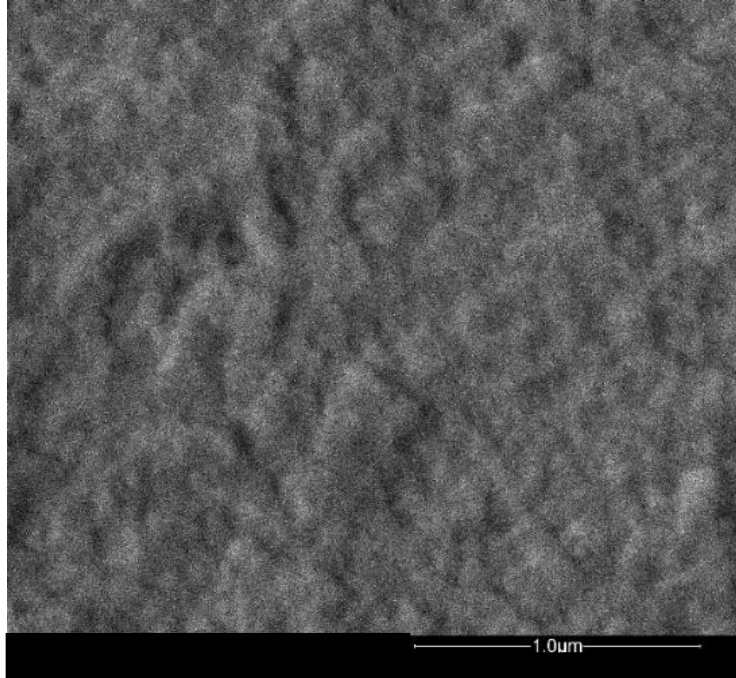
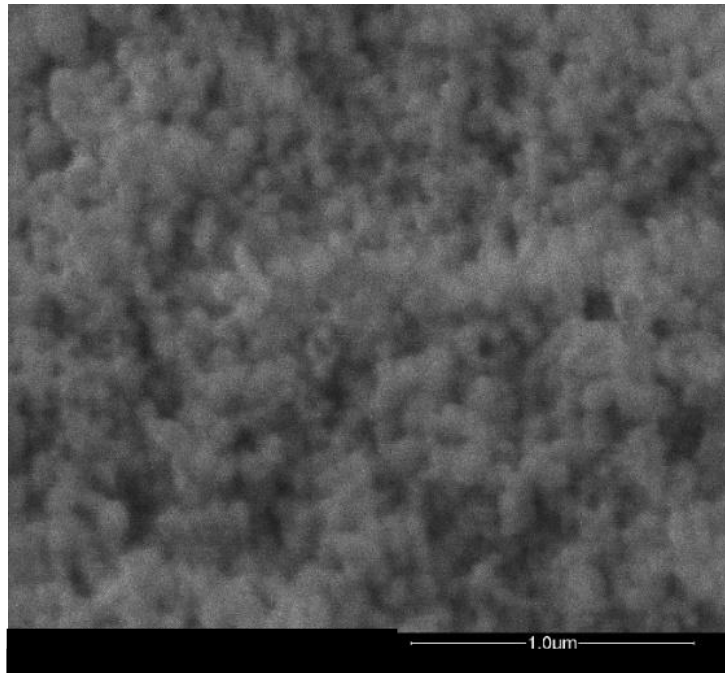


Figure 16: Cumulative pore volume as estimated via gas adsorption testing) vs. estimated pore volume from PECS final relative piston position.



(a) near to the sample surface: exhibiting little to no porosity



(b) near to the sample center: the original particle shape is visible and undeformed

Figure 17: SEM micrographs of sintered microstructure. Variation of features indicate the presence of a thermal gradient in which the sample surface is at a higher temperature than the interior, resulting in a more fully sintered microstructure at the surface than the center of the compact.

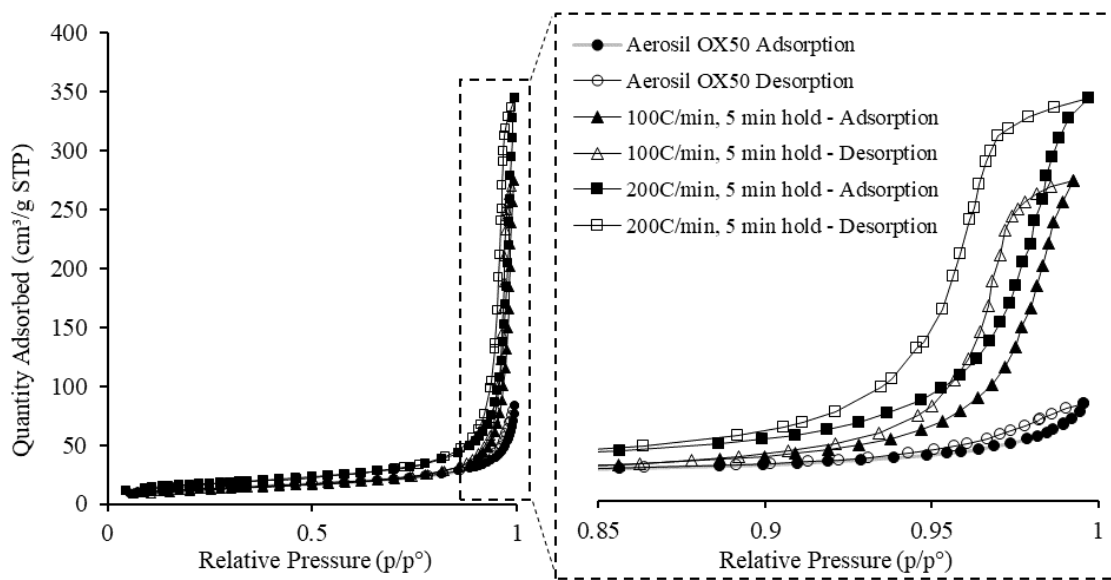


Figure 18: Comparison of N₂ Gas Adsorption Isotherms for Aerosil OX50, and samples processed via PECS to 800 °C with heating rates of 100 °C/min and 200 °C/min. It appears that the sample heated more rapidly has a larger fraction of pore volume, as would be expected.

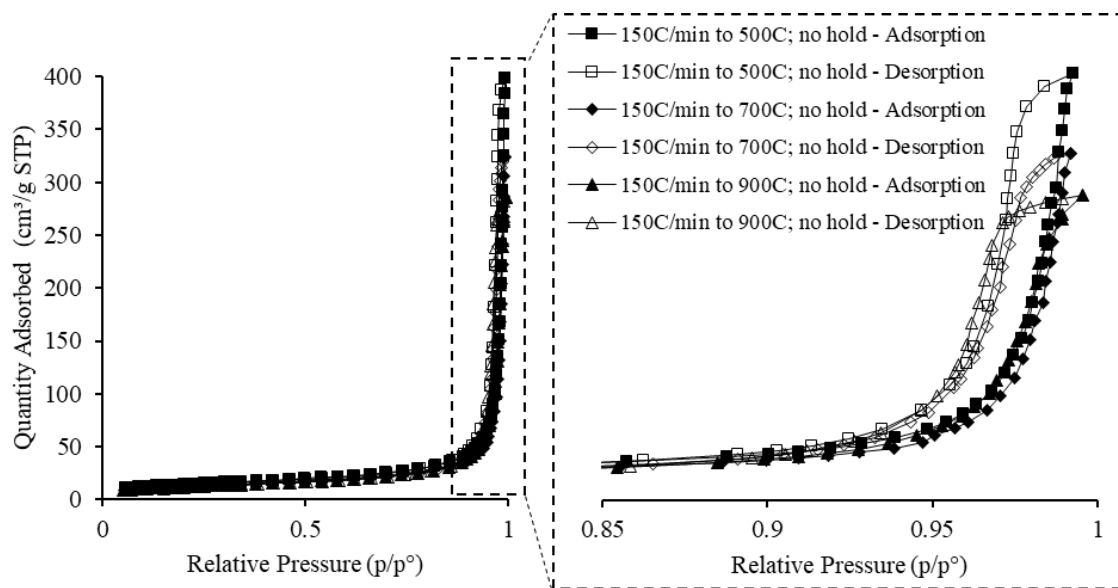


Figure 19: Comparison of N₂ gas adsorption Isotherms for samples sintered at 500 °C, 700 °C, and 900 °C, with a heating rate of 150 °C/min. Samples heated to a higher temperature show a lower fraction of pore volume, as expected. Although the compact sintered at 500 °C showed little vertical shrinkage, it has a noticeably different isotherm than unsintered Aerosil OX50 (see Figure 18).

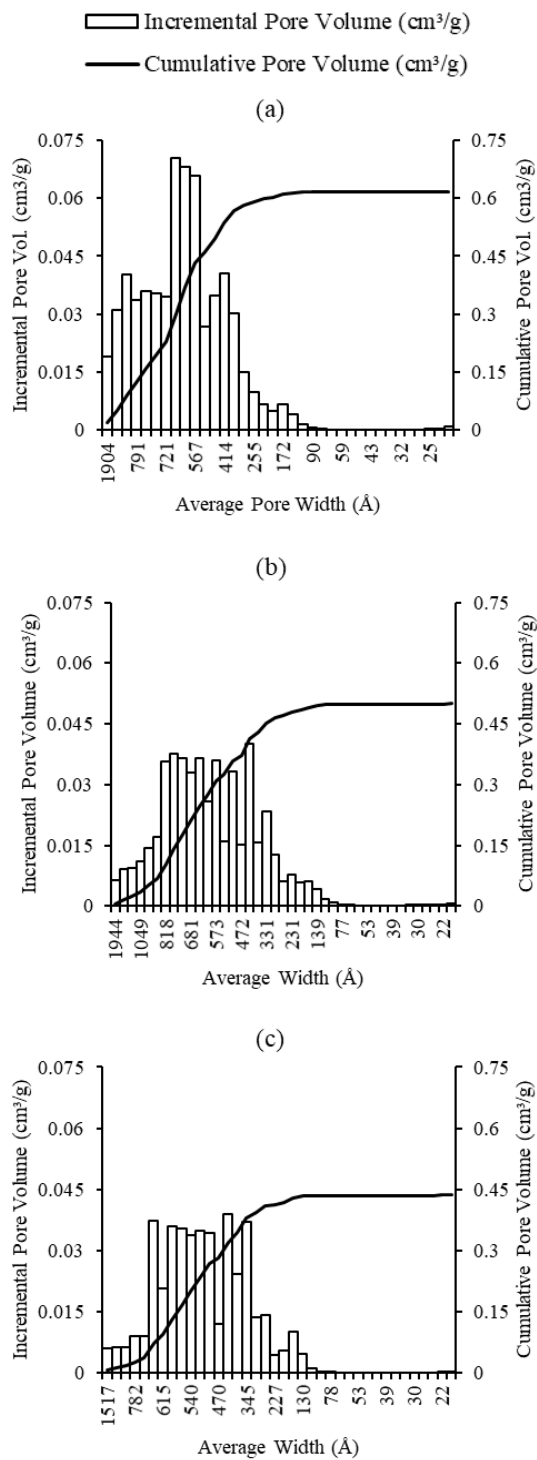


Figure 20: Dollimore-Heale pore distributions; 150 °C/min to (a) 500 °C, no hold (b) 700 °C, no hold (c) 900 °C, no hold. The cumulative porosity of the sample can be seen to decrease with increasing sintering temperature, and the incremental pore volume distribution shifts slightly toward smaller average pore widths.

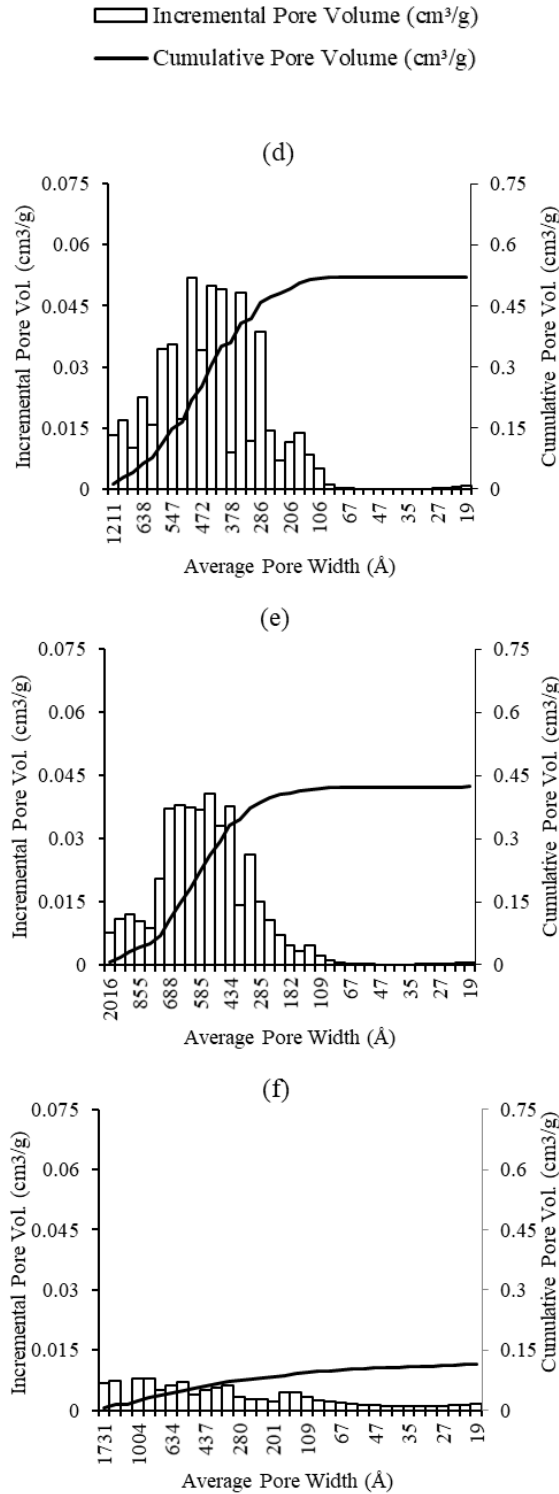


Figure 21: Dollimore-Heale pore distributions vs. heating rate (d) 200 °C/min to 800 °C, 5 minute hold (e) 100 °C/min to 800 °C, 5 minute hold (f) as received (un-sintered). There is a clear decrease in cumulative pore volume when temperature is increased more slowly.

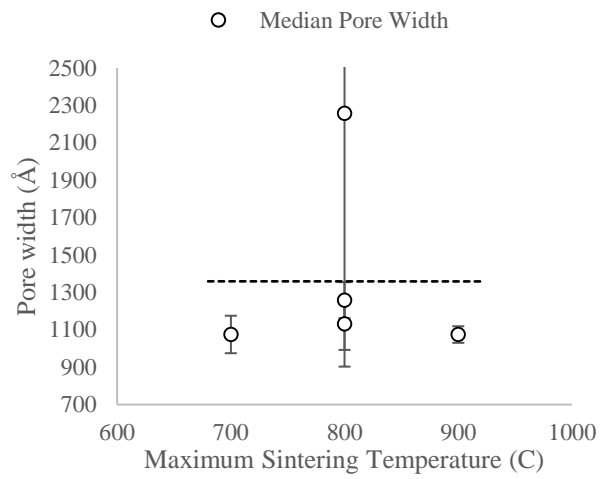
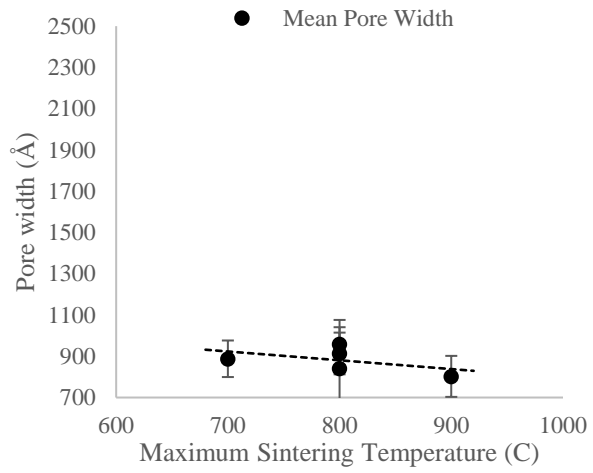


Figure 22: The median pore width does not shift significantly with maximum sintering temperature, though there does seem to be a decrease in mean pore width with increased temperature. These results are likely due to the graded porosity of the sample.

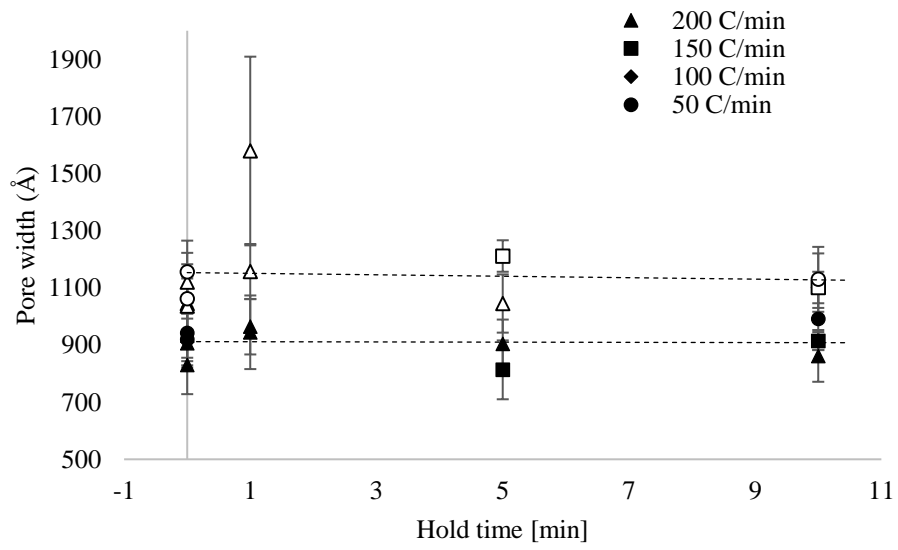


Figure 23: Mean (filled points) and median (open points) pore widths do not change with hold time at max. temperature, for samples held at for up to 10 minutes before cooling.

C. Rapid Fabrication of Fused Glass Specimens Using Pulsed Electric Current Sintering of Amorphous Fumed Silica Nanoparticles

Characteristic consolidation for two different processing temperatures during processing is shown in Figure 24. It is most notable that a rapid densification is observed between 930-1000 °C, indicating softening of the glass to allow viscous flow.

Plotting piston position against temperature allows for improved visualization of sintering during the PECS cycle (Figure 4). It is clear to see that as samples are heated to higher temperatures a greater degree of sintering is achieved.

Curves for maximum temperatures below 900 °C are included here for reference, and these experiments are discussed previously. At 600 °C and below, no significant permanent compression of the sample is observed, indicating that insufficient thermal energy was supplied to facilitate sintering. Upon reaching the temperature where the glass can flow, nominally full consolidation is achieved and no further compression of the samples is observed, even at higher temperatures. The change in relative piston position at this point can be attributed to thermal expansion.

The fusion front follows thermal gradients into the sample, densifying first the surfaces/edges, and then progressing into the center of the sample. This is portrayed schematically in Figure 14. Bubbles are forced out of the center of the sample as the fusion front progresses, but the removal of the large pores is hindered by the complete fusion of the edges of the samples, due to proximity to the die walls. Once the outside edges are “sealed” removal of trapped gas must proceed by diffusion through the glass matrix.

FTIR spectra for the unprocessed Aerosil OX 50 silica powder, and samples sintered at 800 °C, and 1100 °C are given in Figures 8, 15, and 26, respectively.

As previously discussed, the starting powder is fully saturated with water and silanol groups, as expected. The glass heated to 800 °C has a continuous, open pore microstructure,

and thus a significant surface area populated with surface -OH groups. When temperature increases to the glass transition region, the pore structure collapses, interior surfaces are fused, and pores removed during viscous sintering. The surface silanol groups become internal and the vibration band shifts to a lower wavenumber.

The position and the intensity of the features do not vary once the glass has been heated above T_g , regardless of sintering parameters (heating rate, hold time at temperature set point, pressing force). This indicates that the role water plays in sintering these samples and that removal of water/silanol groups from the glass is not affected by changing the processing parameters.

Unlike the results of Rödning, et al.⁵¹, etching of the fracture surfaces did not reveal a granular microstructure reminiscent of sintered crystalline materials. Instead, a homogeneous glass surface that was unaltered by the etching process was observed. Sample containing trapped bubbles seemed to etch preferentially at those interior surfaces. Round etch pits were observed in such cases, as seen in Figure 28. This is ascribed to the fact that the starting nanopowder contained a large amount of water, which facilitated sintering and removal of stresses. The fully-fused glass samples have no observable “granule” microstructure, as the difference in glass structure between the bulk and boundaries formed from pre-consolidation surfaces of the original particles/agglomerates is negligible.

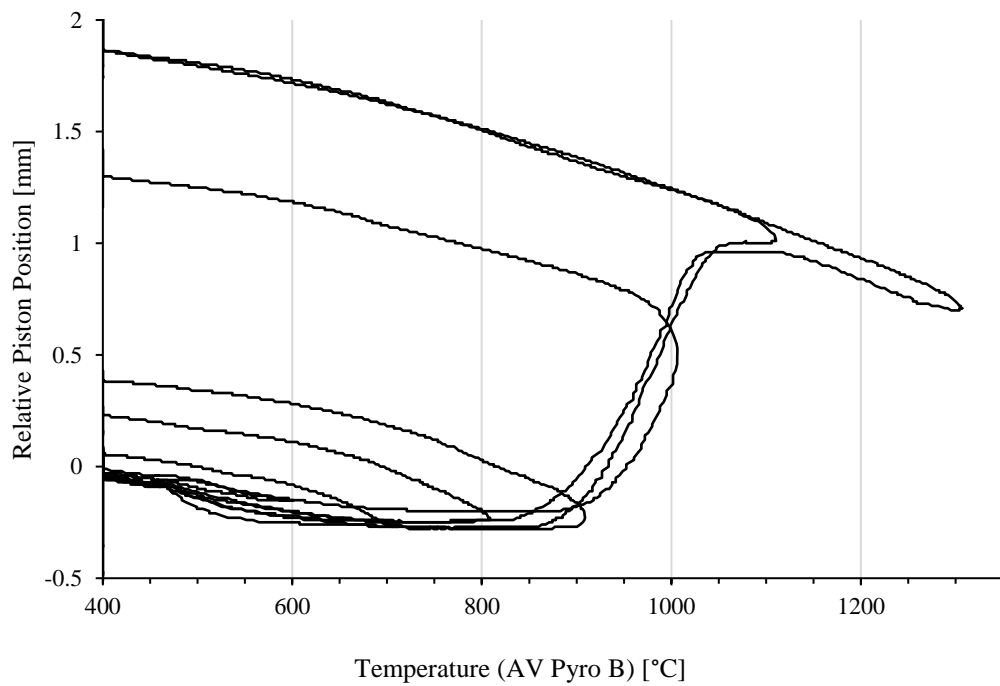


Figure 24: Characteristic consolidation visualized as piston position plotted against temperature. The initial (0 mm) and final piston positions relate to the degree of sintering achieved during heating and cooling. It should be noted that when cooling begins the pressing force is relieved simultaneously.

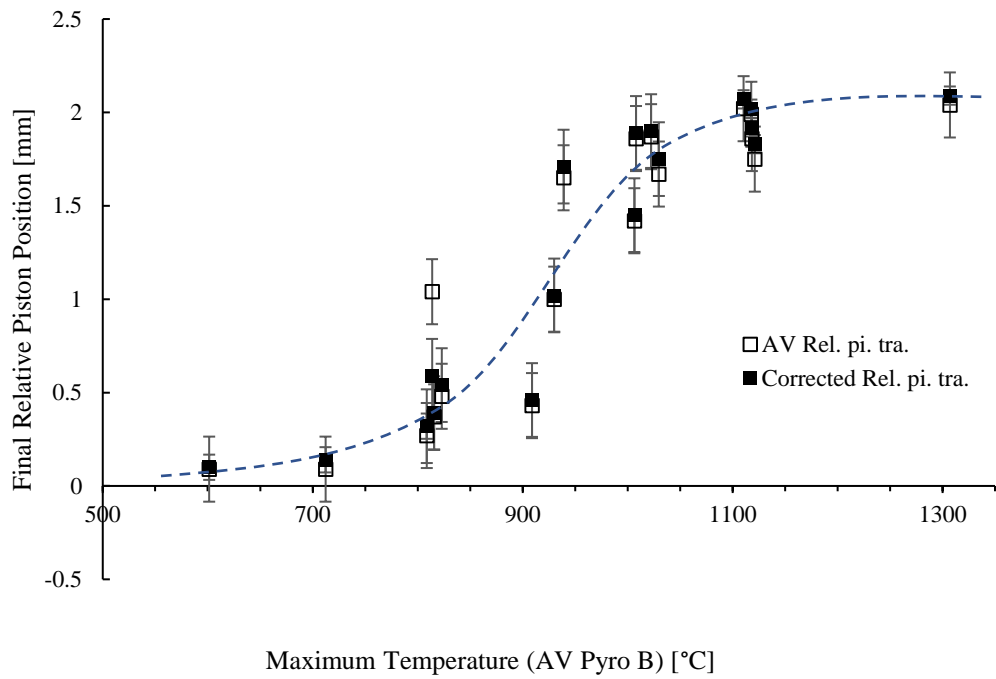


Figure 25: Final relative piston position vs. maximum sintering temperature. A sigmoidal curve is provided as a guide to the eye.

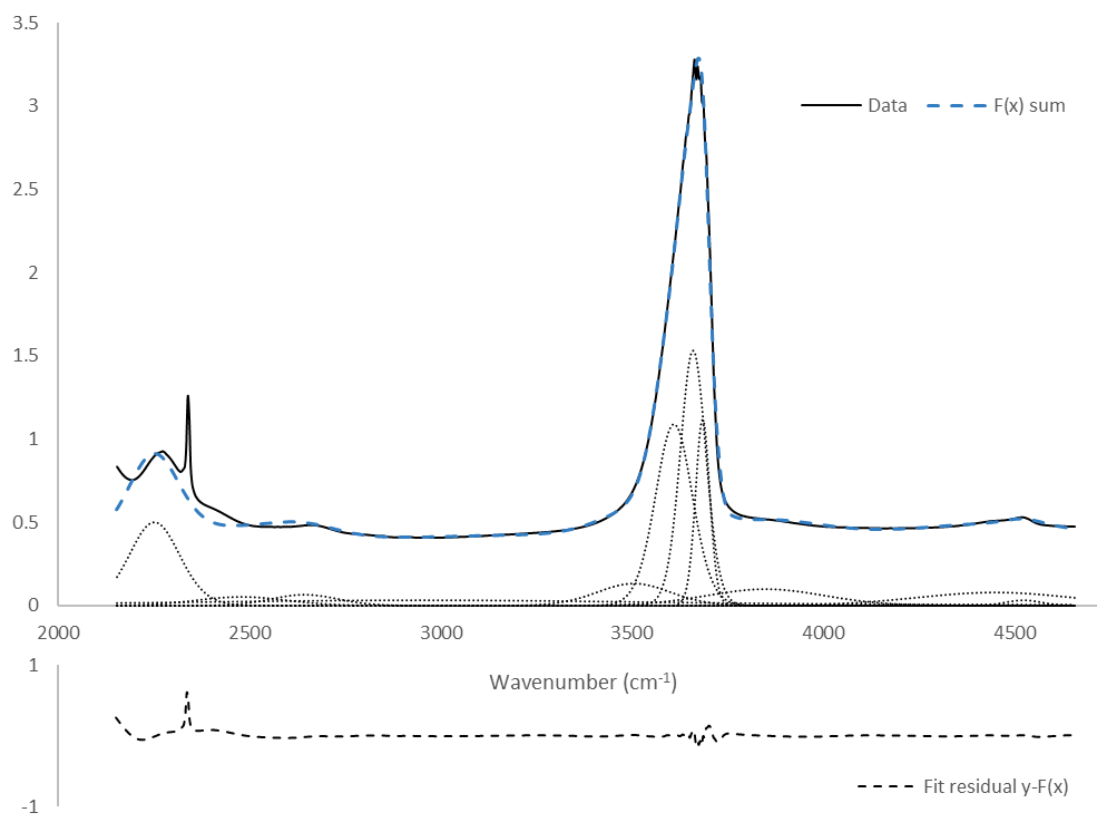


Figure 26: Fitted FTIR Spectrum for Aerosil sintered at 1100 °C. Peak assignments are tabulated in Table 2. The spectrum for the un-sintered powder is given in Figure 8.

Samples heated to 1000 °C (as measured by external pyrometer) and above underwent rapid viscous sintering to form densified glass monoliths, with some notable features. Incomplete consolidation was observed in some samples as the fusion front (Figure 33) moved through the material, resulting in residual bubbles trapped within the bulk of the glass. Many samples underwent varying degrees of crystallization. Cristobalite crystals consistently nucleated at the corners, occasionally on the surface, and in a few cases from within the bulk of the sample. Upon cooling, much of the crystalline phase fractured from the glass due to stress induced by the varying thermal expansion of the phases. SEM investigation also shows what appears to be the crystalline phase pulling away from the glass to create voids (Figure 29).

Optical micrographs exhibiting typical examples of these features are given in Figure 30. Samples with longer holding times at the maximum temperature tended to have a higher degree of crystallization, but this was not always the case.

As it was impossible to do so quantitatively, the extent of surface devitrification, bulk and/or surface devitrification, and trapped bubbles present in each sample was qualitatively ranked from none to extreme for all samples heated to 1100 °C. A schematic describing this ranking system is shown in Figure 31, and the results are plotted against heating rate in Figure 32. No correlation was found between heating rate and any of the mentioned defects, but a positive association between the extent of edge and bulk devitrification was noted (Pearson coefficient of $r \sim 0.7$). There was a small negative association between the presence of trapped bubbles and devitrification ($r \sim -0.25$).

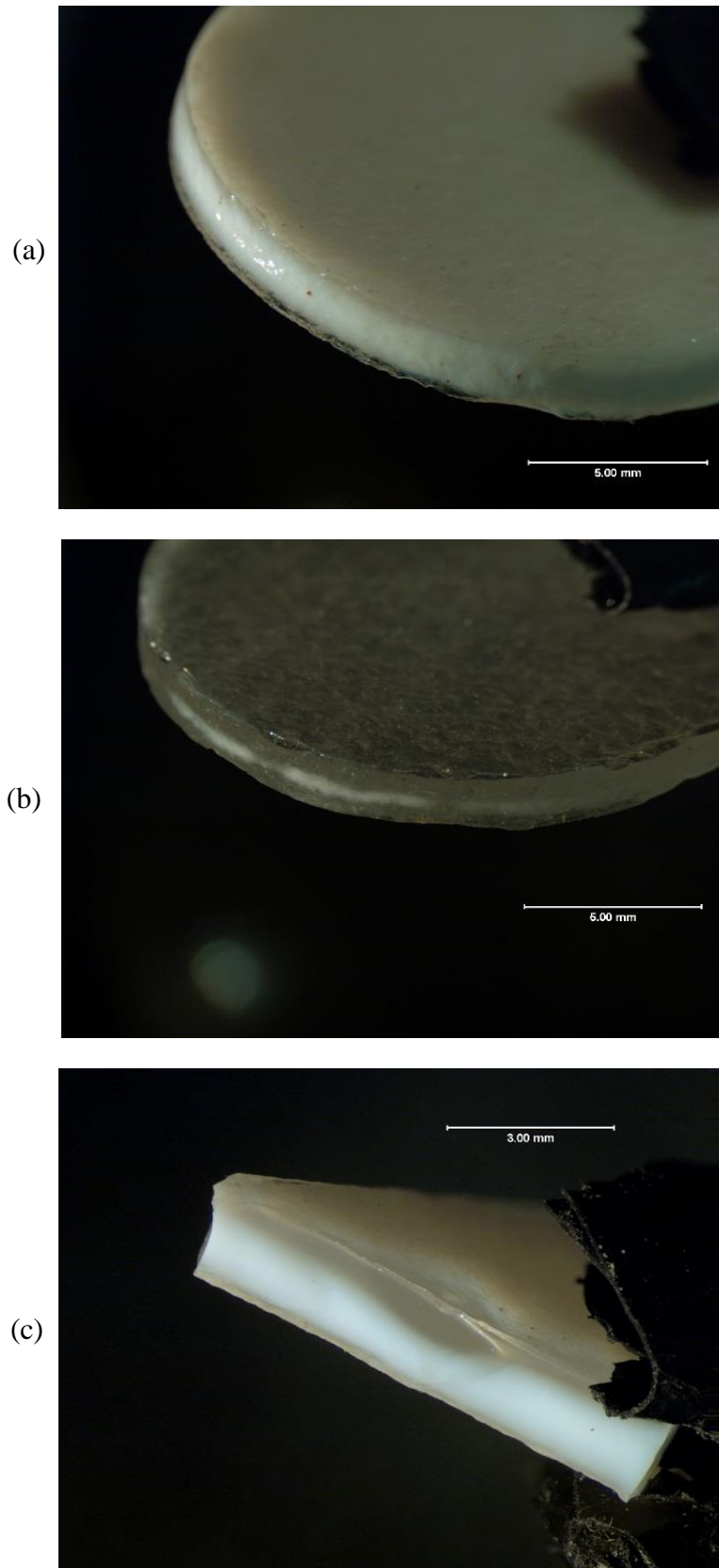


Figure 27: Optical micrographs of samples heated to (a) 1000 °C (b) 980 °C (c) 940 °C

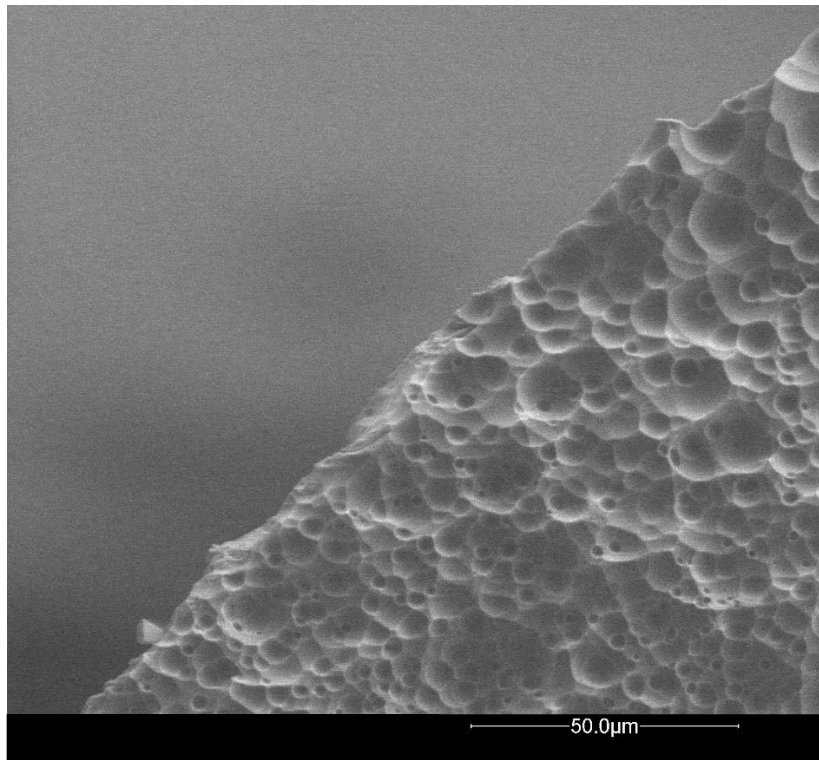
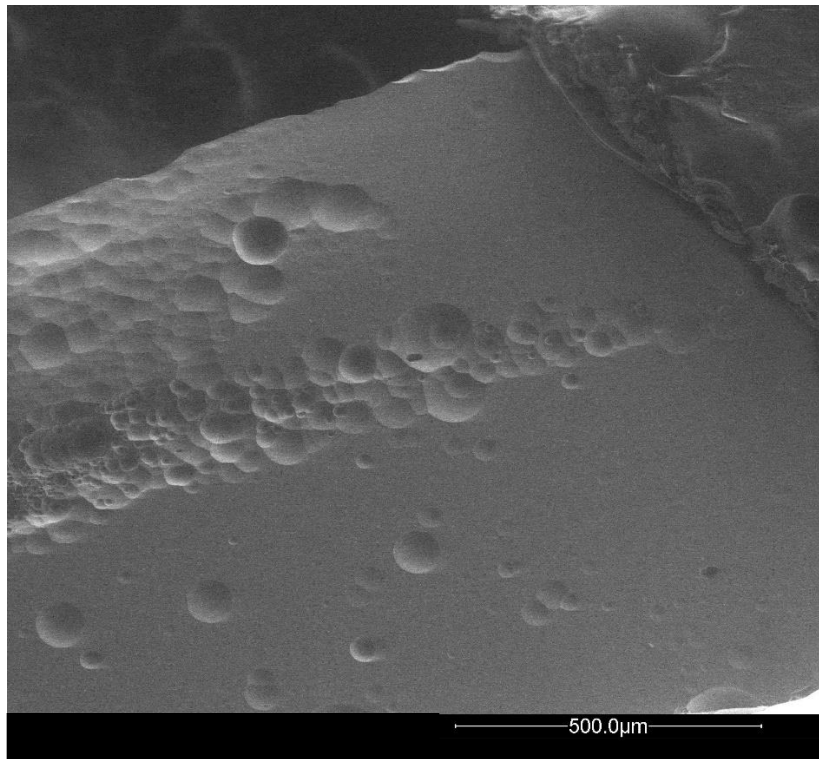
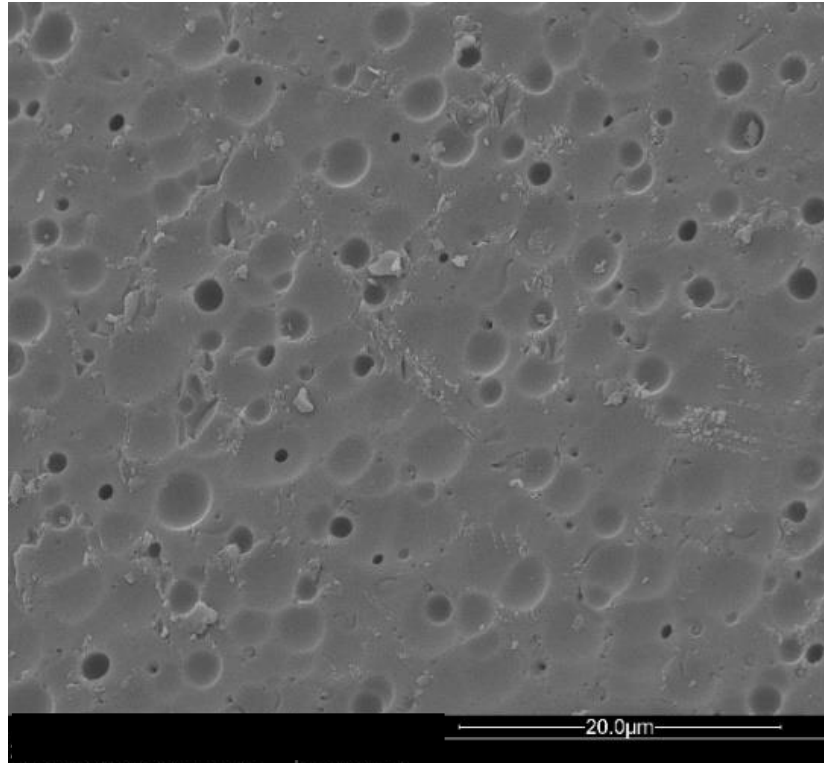


Figure 28: SEM micrographs of sample fracture surfaces etched in 17% HF for 24 hours

(a)



(b)

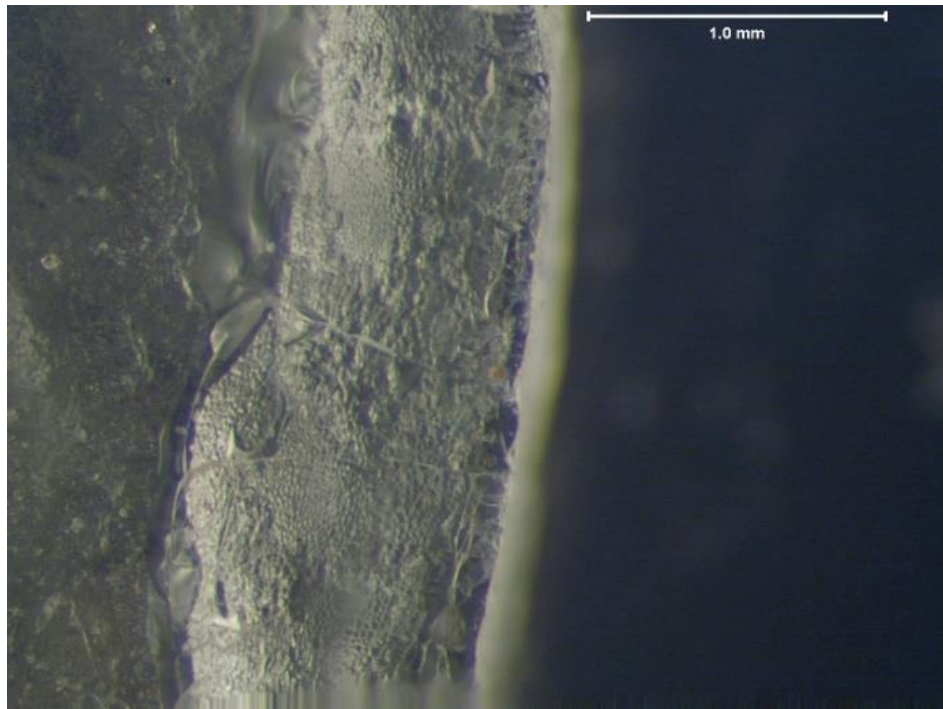


Figure 29: Voids and texture at fracture surface between glassy and crystalline phase.
(a) SEM micrograph; (b) Composite optical micrograph.

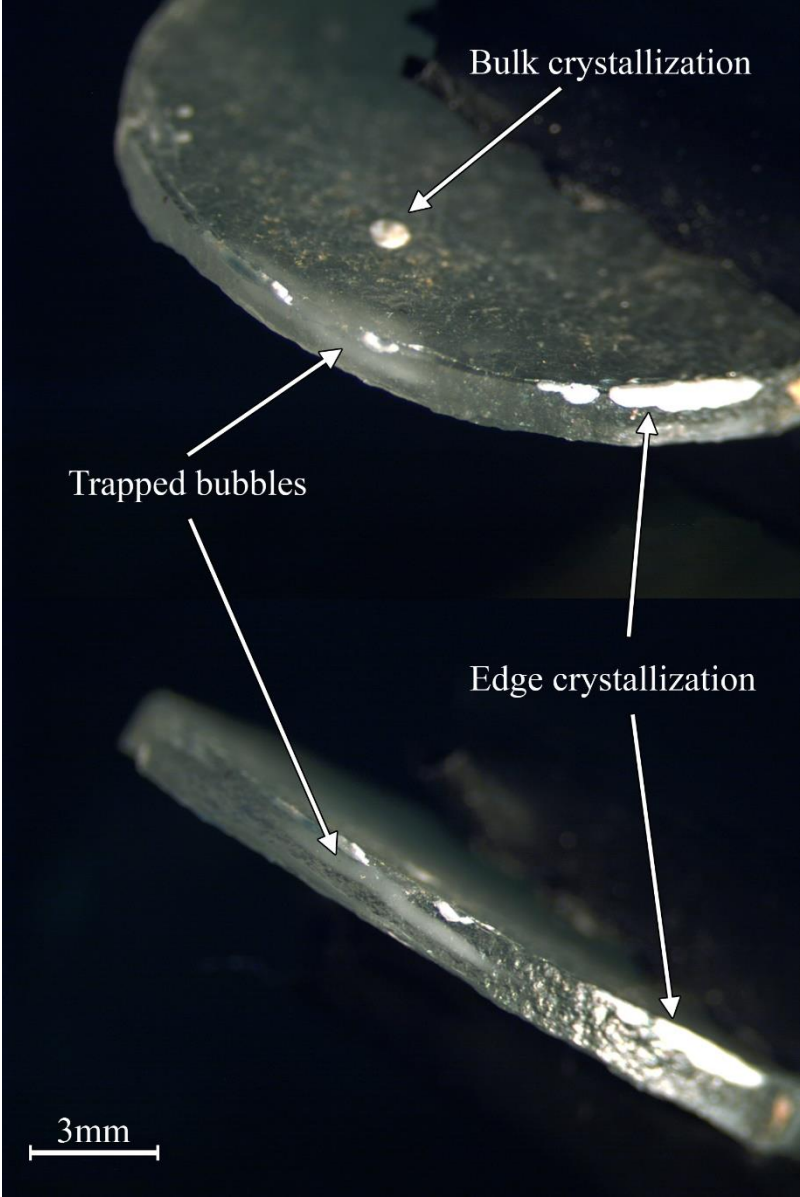


Figure 30: Examples of common macroscopic defects in fused glass specimens.

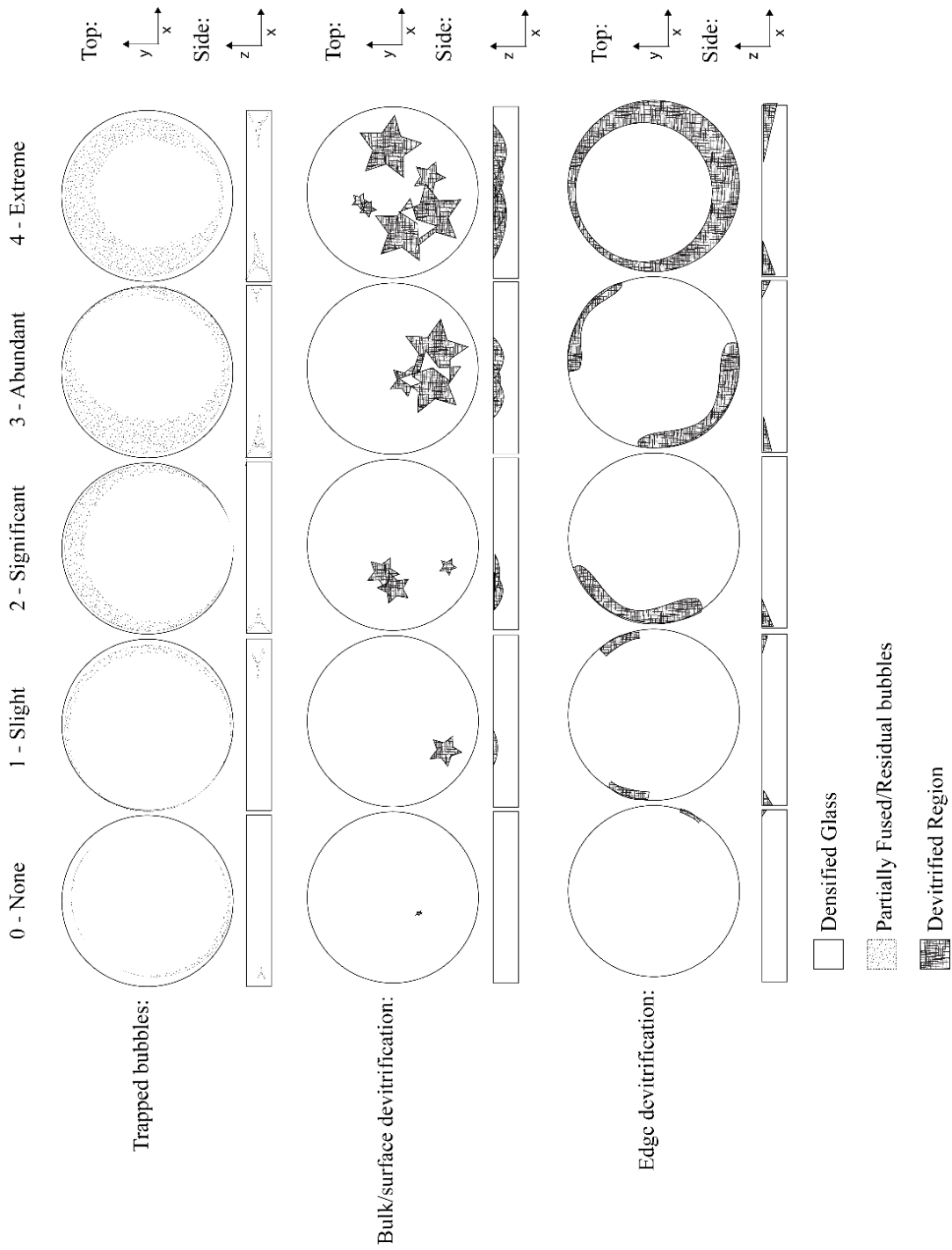


Figure 31: Ranking system for flaws in samples.

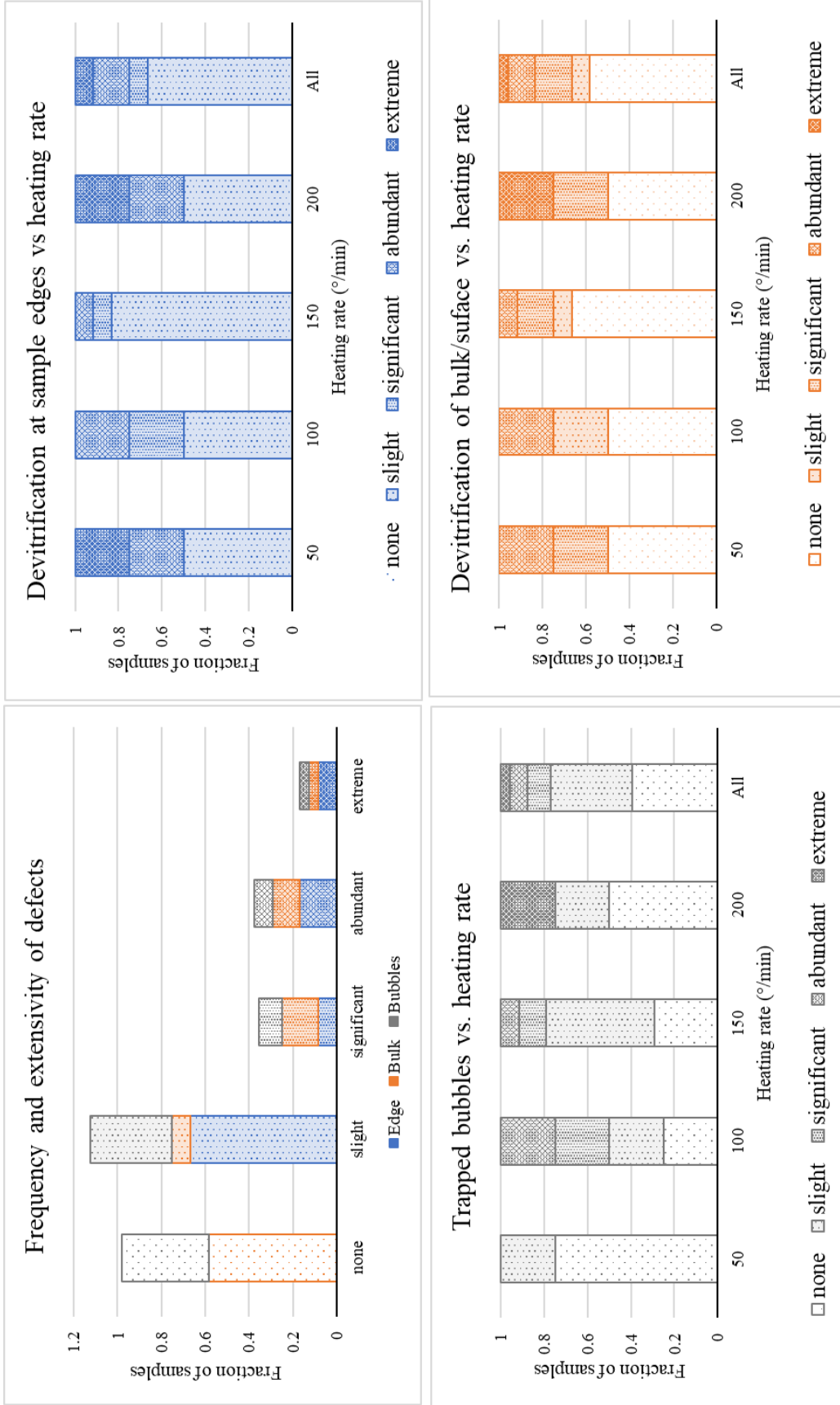


Figure 32: Frequency and extensivity of flaws, and correlation of flaws with heating rate.

The lack of correlation between sample defects (devitrification, trapped bubbles) and processing variables, such as temperature set point or heating rate, implies that there is a lack of precision inherent in sintering materials this way, despite care being taken to reduce processing variables. This is not unexpected, considering that the samples are heated and cooled rapidly, and so spend only short minutes in the temperature window for rapid fusion. In fact, the majority of consolidation is achieved in mere seconds. A related observation is that devitrification must occur during the short window in which the sample is provided sufficient thermal energy to facilitate the phase transition. This is much more rapid than the time-scale typically observed for the transition of amorphous silica to cristobalite at comparable temperatures.

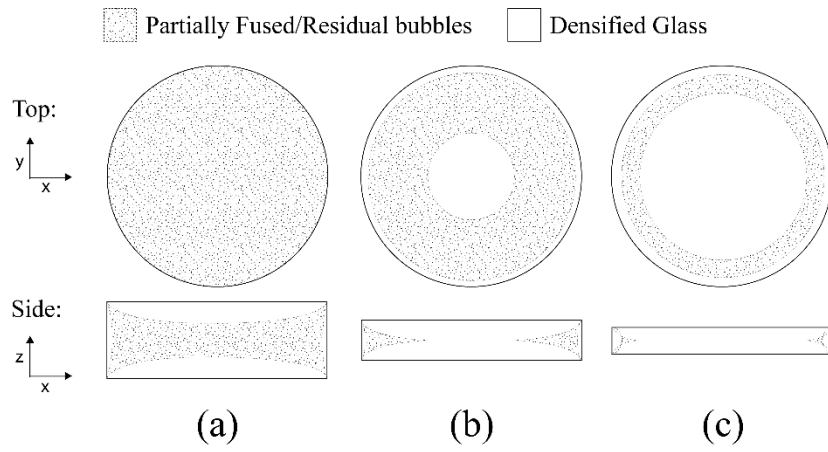


Figure 33: Schematic of the progression of the fusion front into the glass powder compact.

D. On the Effect of Pressing Force on Consolidation of Fumed Silica Powder using Pulsed Electric Current Sintering

As previously discussed, glass powders are known to fuse according to simple viscous sintering models which are dependent on the ability of the glass to flow at a given temperature. Applying a significant pressing force, as is commonly utilized with PECS, activates additional sintering mechanisms, resulting in simultaneous occurrence of enhanced densifying mechanisms, particle rearrangement, and plastic deformation. The extent of these additional consolidation mechanisms is directly related to the applied force, and the associated stress experienced by the material. In general, and particularly because of the nature of the material, it is very difficult to distinguish between simultaneously occurring viscous flow, diffusion, and plasticity mechanisms when considering deformation of a glass.

Figure 34 shows optical micrographs of several samples processed with increased pressing force. All samples obtained were free of bubbles and experienced little to no devitrification, but small fractures were often present around the edges of the samples. These may have resulted from crystallized portions breaking off of the bulk glass during the β to α cristobalite transformation, or could be an artifact of the increased pressing force. In any case, it appears that increasing the pressing force does suppress devitrification. This would be expected, as complete consolidation was observed to occur at a lower temperature (measured at the external die wall by optical pyrometer) as axial pressing force is increased.

As before, piston position is plotted against temperature to monitor in-situ the progression of sintering (Figure 35). There is a clear change in the onset of sintering between the samples when pressing force is increased above 10 kN. Rapid consolidation in the samples pressed to 15-30 kN appears to begin about 100 °C below those only under 5-10 kN of force. Following that trend, the powder compacts experiencing 15-30 kN are fully densified when the optical pyrometer registers about 150 °C lower than those only pressed

to 5-10 kN. As can be seen in Figure 36, aside from the dramatic shift beginning at 15 kN, there does not seem to be significant change in the sintering behavior of the glass.

It is most likely that the increase in applied axial force allows the fumed silica powder to rearrange within the die, resulting in better particle packing and thus more efficient sintering. As temperature increases, plastic deformation is enabled near the softening point of the glass. Above the glass transition, the material flows relatively easily, and applied force simply facilitates viscous flow, and hence the removal of pores from the compact (which can be considered as bubbles within the glass).

By optimizing the pressing force parameter for processing, full consolidation can be achieved at lower temperatures and in a shorter time period, which is of economical advantage. Additionally, increasing pressing force suppresses devitrification, as the phase transformation requires extended time elevated temperatures. The benefits are limited by physical parameters of the experimental set-up but have positive implications for applications in which higher temperatures and the presence of extreme thermal gradients may damage a composite phase, or in which crystallization needs be avoided.

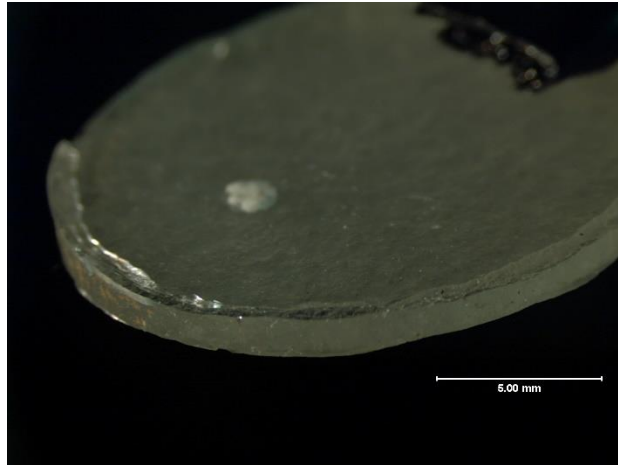
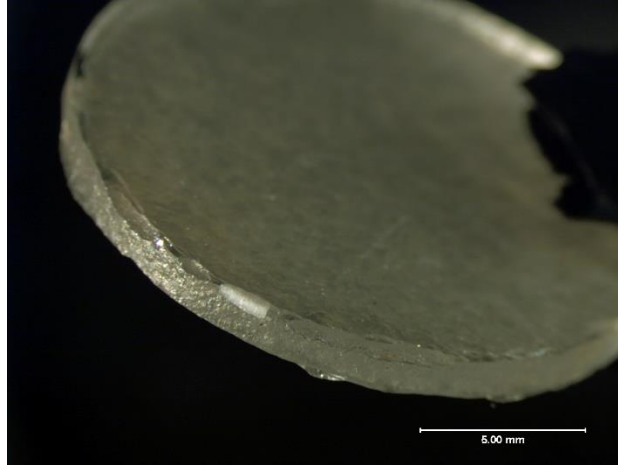


Figure 34: Optical micrographs of PECS samples. All samples obtained were free of bubbles and experienced little to no devitrification, but small fractures were often present around the edges of the samples. These may have resulted from crystallized portions breaking off of the bulk glass during the $\beta \rightarrow \alpha$ cristobalite transformation, or could be an artifact of the increased pressing force.

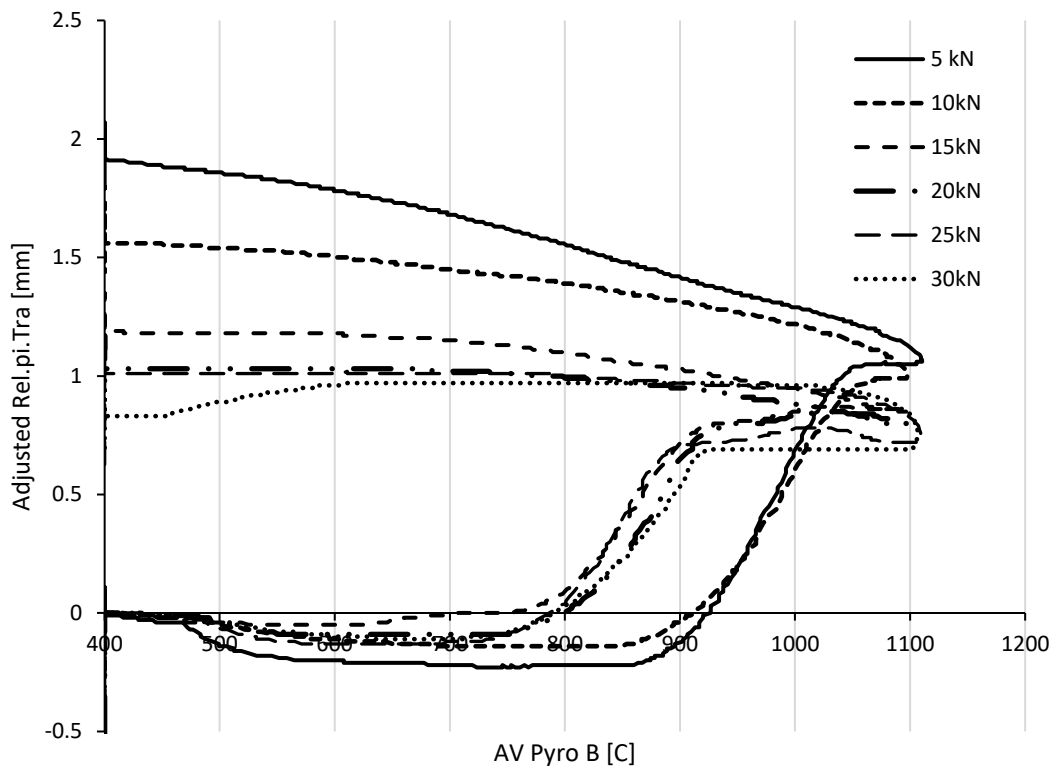


Figure 35: Characteristic consolidation visualized as piston position plotted against temperature. The initial (0 mm) and final piston positions relate to the degree of sintering achieved during heating and cooling. Rapid consolidation in the samples pressed to 15-30kN appears to begin about 100 °C below those only under 5-10kN of force. It should be noted that when cooling begins the pressing force is relieved simultaneously.

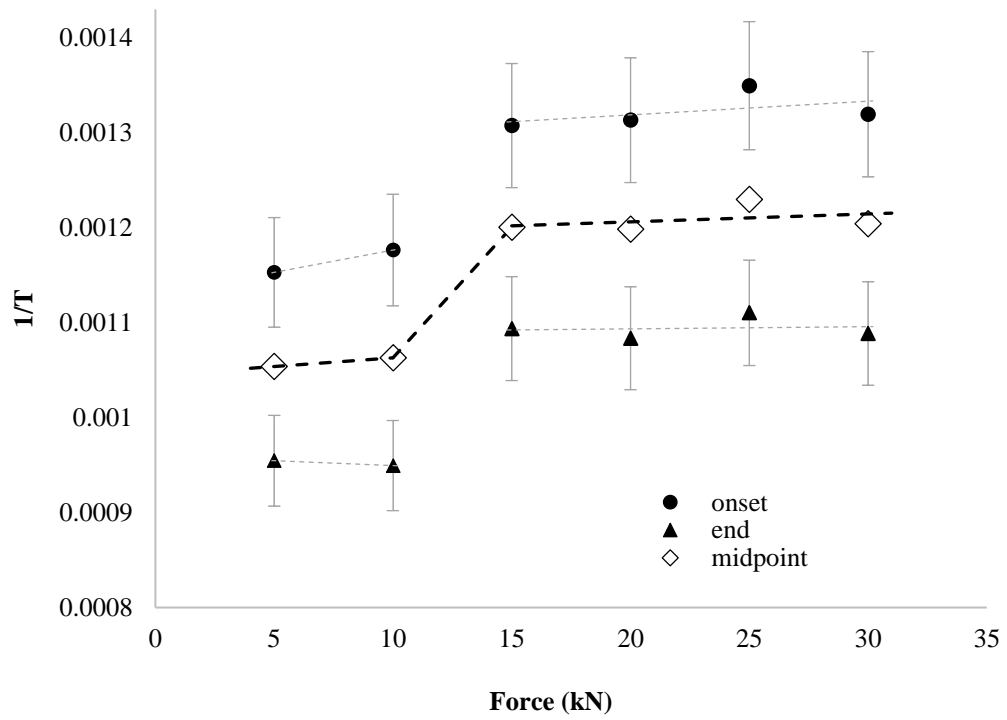


Figure 36: Pressing force vs. onset of sintering and complete consolidation temperatures. Aside from the dramatic shift beginning at 15 kN, there does not seem to be significant change in the sintering behavior of the glass (as inferred from slope).

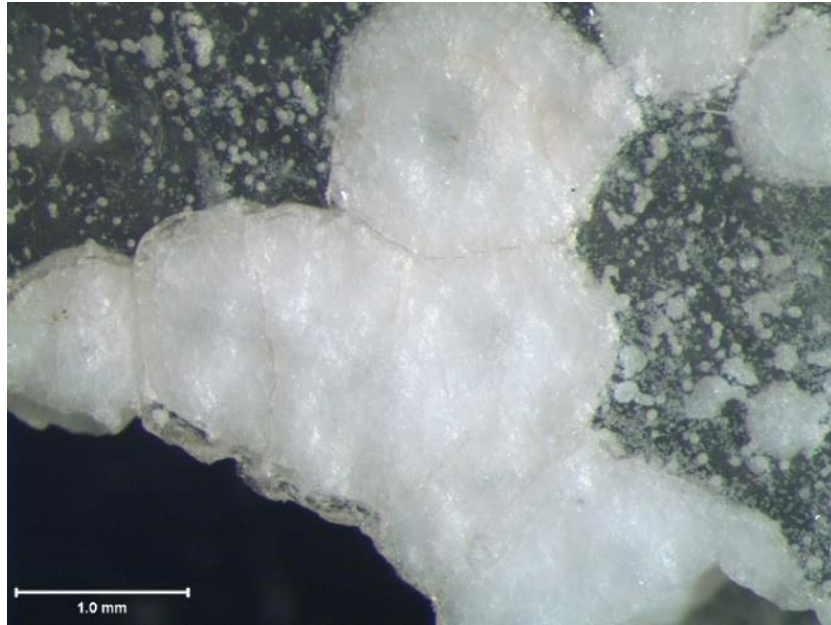
E. Rapid Devitrification of Silica Glass During PECS

All samples heated to above 1000 °C underwent some degree of devitrification, regardless of heating rate, hold time, or maximum temperature. Crystallites grew most often from the surface and corners of the samples and often broke away from the glassy phase, in cases resulting in fracture of the entire sample (Figure 37). The crystalline phase exhibited an unusual, cross-hatched microstructure (Figure 38).

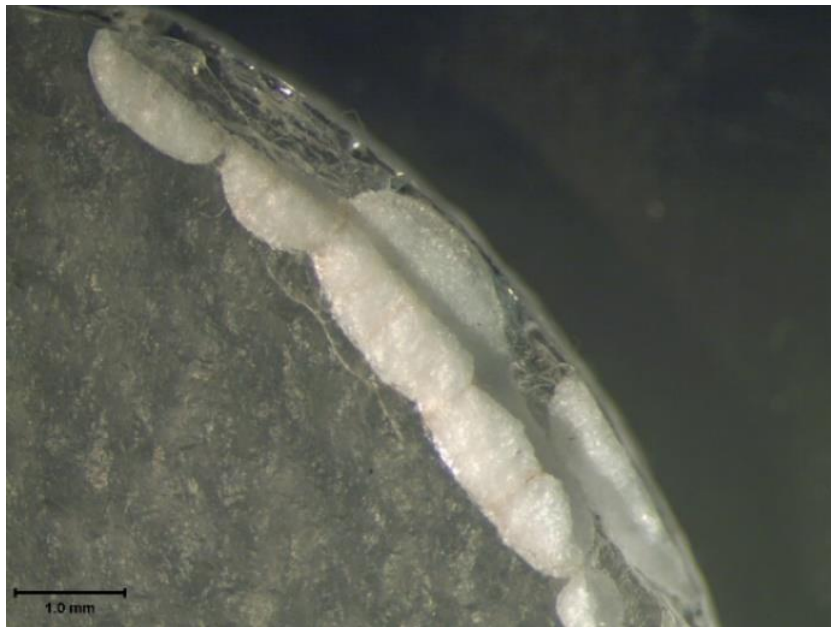
It is unclear whether nucleation of cristobalite occurs before or after full density is achieved. However, circular polycrystalline domains near fracture surfaces, as observed via SEM (Figure 38), suggest that the crystalline phase advanced into the glass and to removed pores along the way. From this observation, it seems likely that crystal growth into the bulk was faster than pore removal. As the fusion front of the glass progresses according to the present thermal gradients, it is also probably that there were no pores remaining at the surfaces at the time devitrification occurred.

X-ray diffraction patterns for bulk and powderized samples of crystalline silica are given in Figure 40. Phase identification of the powder diffraction pattern using the software package Jade 9 (Materials Data Inc.) identifies the crystalline phase as α -cristobalite.

A piece of devitrified sample was removed from the edge of the sample and mounted in putty (as shown schematically in Figure 39). The XRD pattern from this sample gives information about the direction of crystal growth. The predominance of the (112) peak indicated that those planes are approximately parallel to the upward-facing surface, and the notable lack of the $\langle 101 \rangle$ reflections occurs because those planes are closer to perpendicular. Thus, it seems that the crystallites grow normal to the $\langle 101 \rangle$ planes into the bulk glass, which is not unexpected. Historically, oriented or preferential growth of a cristobalite phase from amorphous silica has been attributed to an effect of residual strains in the glass, perhaps augmented in this case by the temperature and stress gradients that exist within powder compact before and during sintering.



(a)



(b)

Figure 37: Optical micrographs with examples of (a) bulk and (b) edge devitrification.

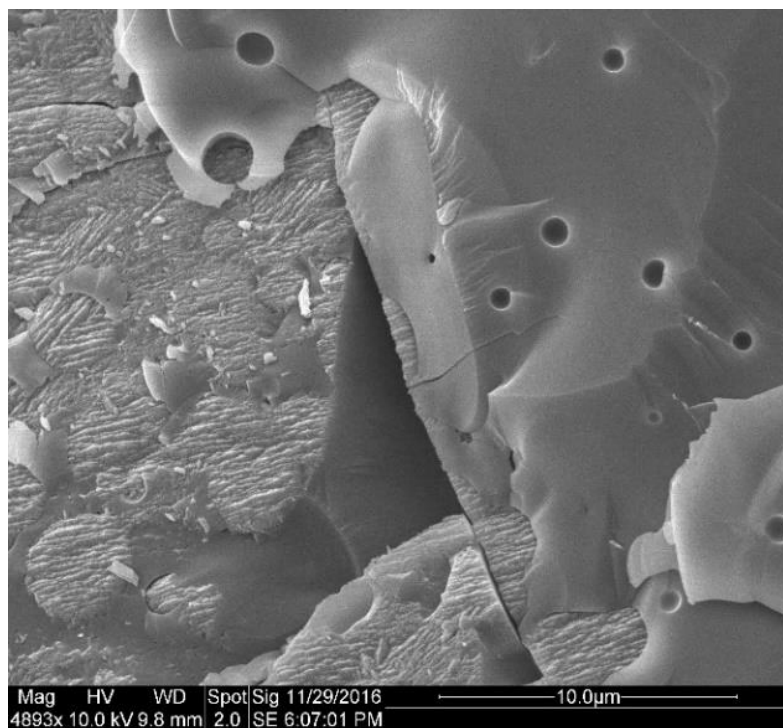
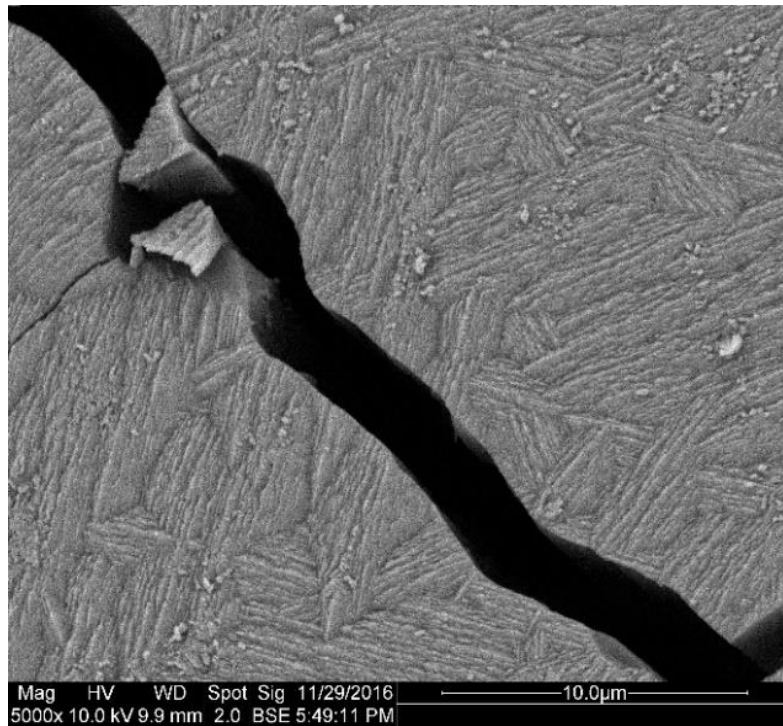


Figure 38: SEM images of fracture surfaces showcasing cristobalite with an unusual, cross-hatched microstructure texture. The presence of round crystalline domains implies that the crystalline phase has grown into the glass more rapidly than pores were removed.

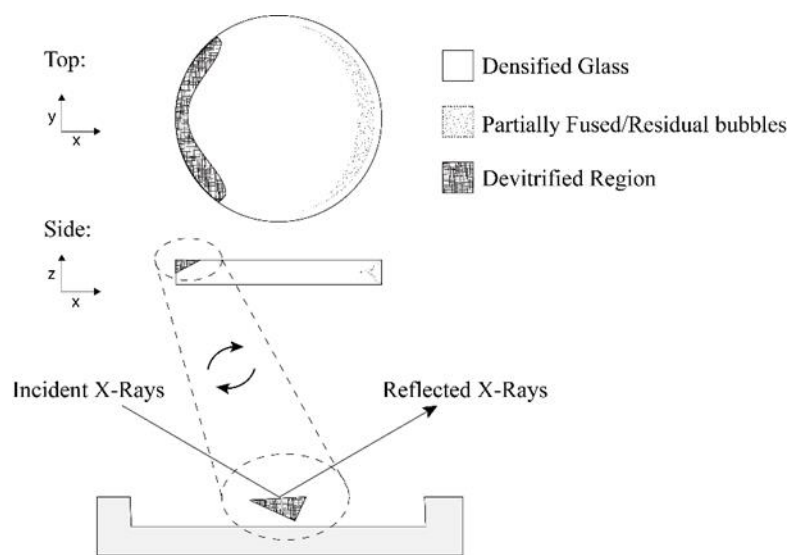


Figure 39: Schematic of devitrified glass and experimental XRD sample configuration and orientation.

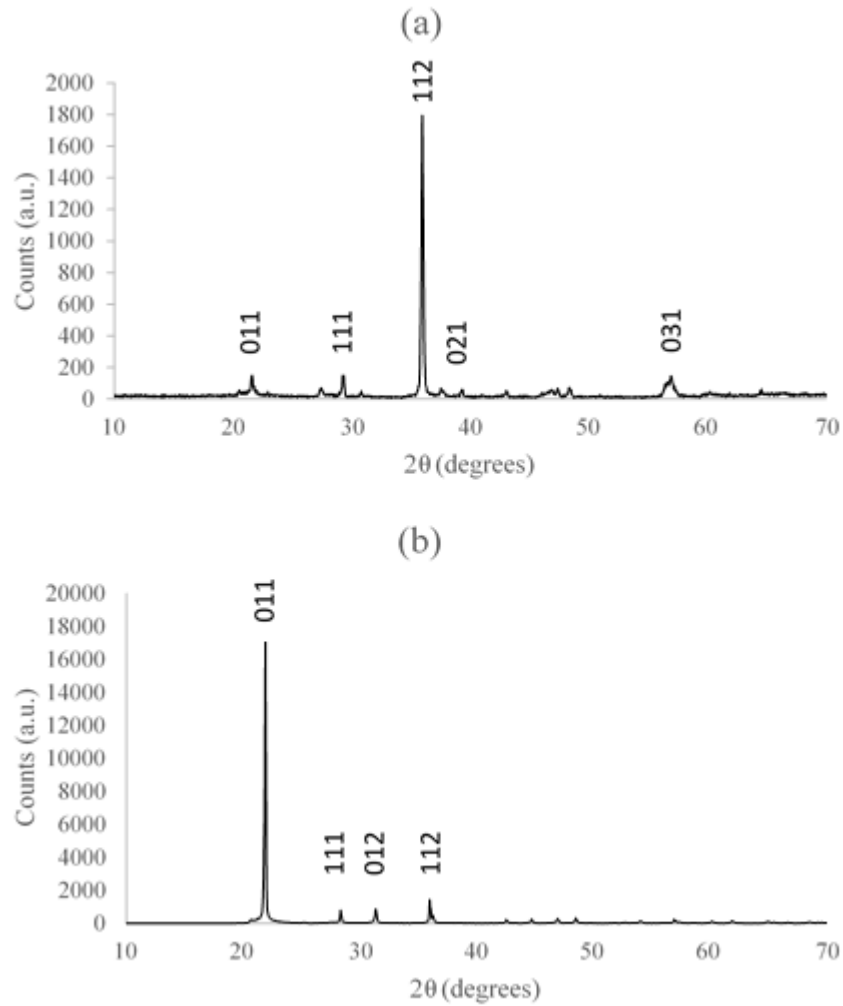


Figure 40: X-ray diffractograms for (a) a chunk of bulk crystalline material (b) crystalline sample that has been pulverized to remove effects of directional growth. Cristobalite planar reflection peaks are labeled.

Inspection of the diffraction patterns identifies the presence of features that cannot be explained by standard Rietveld analysis of the diffraction pattern. Rietveld refinement was performed in TOPAS v4.224 using the Fundamental Parameters⁵⁶ approach for instrumental peak broadening, and a P41212 alpha cristobalite model (Figure 41): red is the measured data, blue is the calculated pattern, and green is the difference between them). The parameters for this refinement are tabulated in Table 4. The clear shoulders on the (011) and (111) diffraction peaks that do not match the refined pattern provide evidence for the presence of stacking faults.

DIFFaX was used to estimate the fraction of the stacking faults by calculating powder diffraction data from a preliminary model for a twin boundary from two layers based on the high temperature polymorph of cristobalite. Parameters for a Pseudo-Voigt function were estimated in order to enable comparison of the simulated data to the laboratory diffraction profile. The fit is given in Figure 42, and fitting parameters reported in Table 4. This model confirms that the shoulders observed in the diffraction pattern correlate to twin boundary defects in the nanocrystalline cristobalite. The stacking fault density as estimated by DIFFaX is about 5%, which corresponds to approximately 1 twin per 8 nm perpendicular to the [111] (trigonal) axis of β -cristobalite.

There are three generally accepted mechanisms by which twinned crystals occur. Twins can form due to a deformation of the lattice during crystal growth, and they can be created spontaneously when a stress is applied to the crystal after it was formed. A crystal that undergoes a phase transformation in which symmetry elements (such as a translation vector, a rotation axis, or an inversion center) are lost will have implicitly defined twin domains. If the energy of creating a stacking fault in a given crystal system is low, such twin defects will likely be commonly observed. Separately, coplanar growth of crystallites can create coherent domains that resemble twins, but do not have an epitaxial relationship and are not considered to be stacking faults.

The phase transformation from β - to α -cristobalite implicitly creates 12 distinct twin domains from loss of symmetry elements (transformation twinning). Thermodynamically, this transformation is troublesome: the high and low temperature polymorphs coexist for an interval of $\sim 20^\circ\text{C}$, and the actual transition temperature has been recorded to vary within

that range. The variation in the transition temperature, and also the hysteresis observed when repeatedly cycling through the phase transformation, is attributed to the available domains in α -cristobalite. Based on this information, one would expect to see prevalent twin boundaries in cristobalite that had precipitated as the high temperature polymorph, which is in fact the case here.

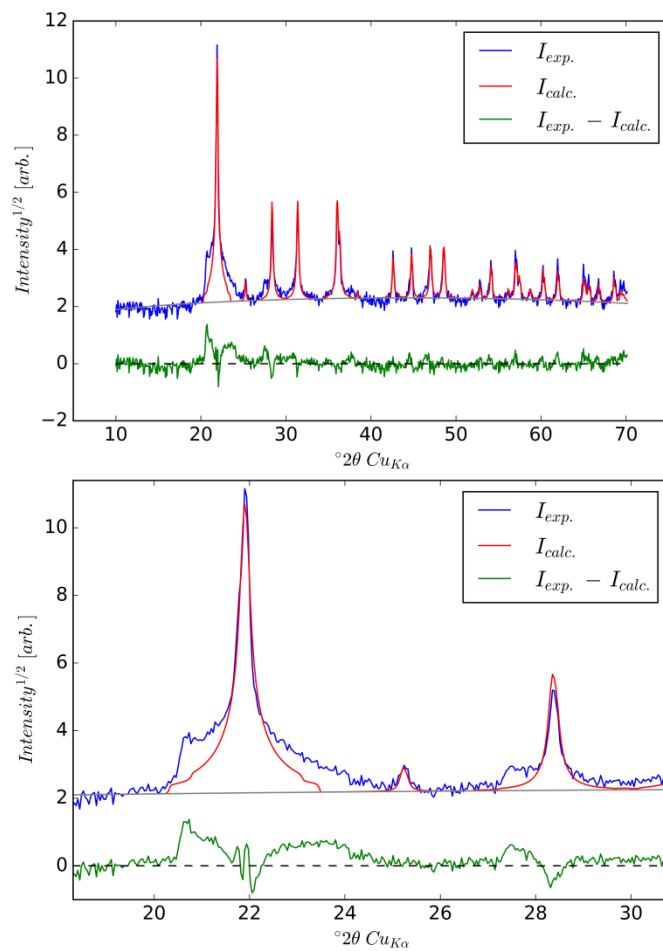


Figure 41: Rietveld refinement of α -cristobalite diffraction profile confirms phase identification (top) ($R_{wp} = 27\%$). Close inspection of the (011) and (111) Bragg peaks at $2\theta = 22.0^\circ$ and 28.5° , respectively, shows evidence for stacking disorder when compared to β -cristobalite model data (bottom).

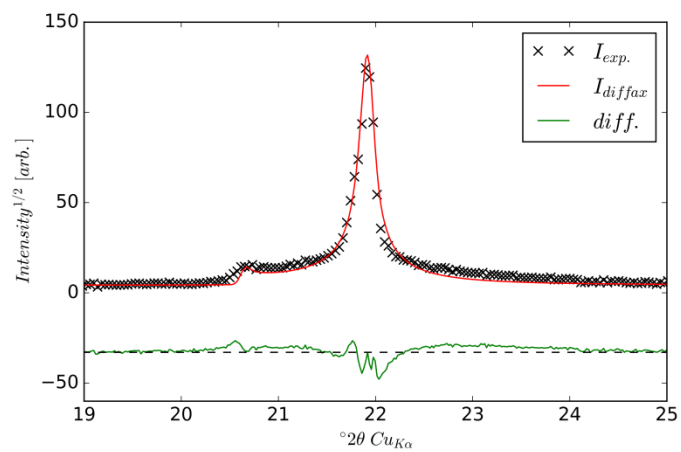


Figure 42: Hand-optimized diffraction profile of the α -cristobalite (011) peak shows evidence for stacking disorder in the low-angle shoulder ($R_{wp} = 23\%$).

Table IV: Tabulated Data for the Rietveld Refinement (TOPAS) and DIFFaX Analysis. Note that DIFFaX has no built-in optimization function, so coefficients for the model were hand-optimized to obtain comparable patterns to those observed in the experimental data.

| <i>Parameter</i> | <i>TOPAS</i> | <i>DIFFaX</i> |
|---|----------------------------------|-------------------|
| <i>S.G.</i> | P4 ₁ 2 ₁ 2 | P1 |
| <i>a</i> [Å] | 4.9727 (4) | 4.9639 |
| <i>c</i> [Å] | 6.9275 (7) | 4.0530 † |
| γ [°] | 120 * | 120. * |
| <i>Si B_{iso}</i> [Å ²] | 6.7 (2) | 0.2 |
| <i>O B_{iso}</i> [Å ²] | 7.5 (3) | 0.2 |
| <i>Lorentzian size</i> [nm] | 104. (7) | - |
| <i>Lorentzian microstrain</i> [] | 0.02 (2) | - |
| <i>microstrian</i> [%] | 0.4 (6) | - |
| <i>R_{wp}</i> [%] | 27 | - |
| <i>n-layers</i> [int.] | - | infinite |
| α_{ii} [frac.] | - | 0.95 |
| α_{ij} [frac.] | - | 0.05 |
| <i>vector 1</i> | - | (1/3, 2/3, 1.0) * |
| <i>vector 2</i> | - | (2/3, 1/3, 1.0) * |
| <i>C_{ij}</i> [Å ²] | - | 0 * |
| † <i>constrained</i> | | |
| * <i>fixed</i> | | |

VI. CONCLUSIONS AND FUTURE WORK

This work reviews critically the potential application of PECS sintering to rapidly produce both fully fused and partially sintered porous, amorphous SiO₂ compacts from powder precursors. Unfortunately, the implicit non-isothermal and inhomogeneous nature of the PECS method are complicit in rendering results that are difficult to reproduce. No correlation was found between heating rate or holding time and any features in the fused samples, even though dependence of the viscosity, and thus the rate of sintering, on temperature would predict an effect of those variables on powder consolidation. Further, The presence of defects and inhomogeneities in all samples implies that the current instrument design is not suitable for consistently processing silica parts.

Critically, early-stage sintering onset temperature was found to vary by ± 35 K for identically prepared samples due to inconsistency of thermal gradients within the die ensemble. This variability makes comparison and robust interpretation of results impossible without improved instrumentation and/or statistical methods. There is a need for an alternative method to measure sample temperature in-situ, or a complementary analytical approach to extract useful information with reasonable confidence from the data.

Cristobalite appears in the samples produced in this work significantly sooner than would be expected, regarding both timescale and activation temperature as typically reported in the literature. Thermal gradients present within the die cause the sample to experience temperatures 100-200 °C higher than those measured at external die wall. The presence of thermal gradients also results in a stress gradient across the sample, contributing to devitrification and the preferential growth direction of the precipitating cristobalite phase.

In order to fabricate silica glass parts using PECS, a balance must be found regarding processing parameters that eliminate unwanted entrained porosity and devitrification, both of which are dependent on temperature gradients and equilibration within the die. According to the TTT diagram, a temperature window should exist within which rapid fusion of glass particles can occur by viscous flow but crystallization is not activated. Such control was not found to be feasible in this work. In practice, any applied approach to

achieving ideal silica glass parts must design suitable control over thermal gradients within the die ensemble. In practice, however, the extreme thermal gradients within the die ensemble removed this possibility.

Processing pure silica glass this way will likely always result in the flaws discussed due to its tendency to form crystalline polymorphs and its high glass transition temperature. However, applying PECS to a more stable glass composition will likely give the desired result: near-net-shape forming of dense, transparent parts, or a controlled porous microstructure in a glass. Despite the challenges reported here, PECS remains an attractive route towards rapid fabrication of glass compacts in general.

To address the issue of thermal gradients in this work, an advantageous study could entail computer modeling of current flow and temperature distributions through various die geometries. It is possible that the extreme thermal gradients as encountered in this work could be reduced in intensity or removed nearly completely by changing the die configuration. Repeating these sintering experiments with an alternative means of measuring temperature, such as via a thermocouple inserted into the wall of the die, would provide more useful data overall and allow better control of the program.

VII. REFERENCES

1. Evonik Industries AG, *Technical Overview: Aerosil® - Fumed Silica* (8th ed.). Hanau-Wolfgang, DE. Available at <aerosil.com>
2. G. W. Scherer, "Sintering of Low-Density Glasses: I, Theory," *J. Am. Ceram. Soc.*, **60** [5-6] 236-9 (1977).
3. G. W. Scherer and D. L. Bachman, "Sintering of Low-Density Glasses: II, Experimental Study," *J. Am. Ceram. Soc.*, **60** [5-6] 239-43 (1977).
4. G. W. Scherer, "Sintering of Low-Density Glasses: III, Effect of a Distribution of Pore Sizes," *J. Am. Ceram. Soc.*, **60** [5-6] 243-6 (1977).
5. G. W. Scherer and J. C. Luong, "Glasses from Colloids," *J. Non-Cryst. Solids*, **63** [1-2] 163-72 (1984).
6. J. Mackenzie and R. Shuttleworth, "A Phenomenological Theory of Sintering," *Proc. Phys. Soc., London, Sect. B*, **62** [12] 833 (1949).
7. J. Ross, W. Miller, and G. Weatherly, "Dynamic Computer Simulation of Viscous Flow Sintering Kinetics," *J. Appl. Phys.*, **52** [6] 3884-8 (1981).
8. A. Jagota and P. Dawson, "Micromechanical Modeling of Powder Compacts—I. Unit Problems for Sintering and Traction Induced Deformation," *Acta Metall.*, **36** [9] 2551-61 (1988).
9. J. I. Martínez-Herrera and J. J. Derby, "Viscous Sintering of Spherical Particles Via Finite Element Analysis," *J. Am. Ceram. Soc.*, **78** [3] 645-9 (1995).
10. A. Jagota and G. W. Scherer, "Viscosities and Sintering Rates of Composite Packings of Spheres," *J. Am. Ceram. Soc.*, **78** [3] 521-8 (1995).
11. M. N. Rahaman, "Theory of Solid-State and Viscous Sintering". *Ceramic Processing*. CRC Press, Boca Raton, FL, 2006. 466-536.
12. P. P. Bihuniak, "Effect of Trace Impurities on Devitrification of Vitreous Silica," *J. Am. Ceram. Soc.*, **66** [10] 188-189 (1983).

13. F. Wagstaff, "Crystallization Kinetics of Internally Nucleated Vitreous Silica," *J. Am. Ceram. Soc.*, **51** [8] 449-53 (1968).
14. F. Wagstaff, "Crystallization and Melting Kinetics of Cristobalite," *J. Am. Ceram. Soc.*, **52** [12] 650-4 (1969).
15. X. Li, X. Yin, L. Zhang, and S. He, "The Devitrification Kinetics of Silica Powder Heat-Treated in Different Conditions," *J. Non-Cryst. Solids*, **354** [28] 3254-9 (2008).
16. R. C. Breneman and J. W. Halloran, "Kinetics of Cristobalite Formation in Sintered Silica," *J. Am. Ceram. Soc.*, **97** [7] 2272-8 (2014).
17. M. L. F. Nascimento and E. D. Zanotto, "Mechanisms and Dynamics of Crystal Growth, Viscous Flow, and Self-Diffusion in Silica Glass," *Phys. Rev. B*, **73** [2] 024209 7pp (2006).
18. M. O. Prado, E. B. Ferreira, and E. D. Zanotto, "Sintering Kinetics of Crystallizing Glass Particles. A Review," *Ceram. Trans.*, **170**, 163-79 (2005).
19. M. O. Prado and E. D. Zanotto, "Glass Sintering with Concurrent Crystallization," *C. R. Chim.*, **5** [11] 773-86 (2002).
20. V. Swamy, S. K. Saxena, B. Sundman, and J. Zhang, "A Thermodynamic Assessment of Silica Phase Diagram," *J. Geophys. Res.: Solid Earth*, **99** [B6] 11787-94 (1994).
21. A. Navrotsky, "Thermochemistry of Crystalline and Amorphous Silica," *Rev. Mineral. Geochem.*, **29** [1] 309-29 (1994).
22. P. J. Heaney, "Structure and Chemistry of the Low-Pressure Silica Polymorphs," *Rev. Mineral. Geochem.*, **29** [1] 1-40 (1994).
23. R. Brückner, "Properties and Structure of Vitreous Silica. I," *J. Non-Cryst. Solids*, **5** [2] 123-75 (1970).

24. F. Wagstaff and K. Richards, "Kinetics of Crystallization of Stoichiometric SiO₂ Glass in H₂O Atmospheres," *J. Am. Ceram. Soc.*, **49** [3] 118-21 (1966).
25. M. Suárez, A. Fernández-Camacho, J. L. Menéndez, and R. Torrecillas, "Challenges and Opportunities for Spark Plasma Sintering: A Key Technology for a New Generation of Materials," Ch.13 in *Sintering Materials*. Edited by B. Ertug. InTechOpen, London, UK, 2013. DOI: 10.5772/56064
26. B. Barazani and D. Torikai, "Spark Plasma Sintering of Silica Glass: Experimental Study on the Temperature Distribution and the Influence of the Heating Rate on Bubble Formation," *Glass Technology-European Journal of Glass Science and Technology Part A*, **57** [3] 89-94 (2016).
27. S. Grasso, Y. Sakka, and G. Maizza, "Electric Current Activated/Assisted Sintering (ECAS): A Review of Patents 1906–2008," *Sci. Technol. Adv. Mater.*, **10** [5] 053001 24pp (2009).
28. O. Guillon, J. Gonzalez-Julian, B. Dargatz, T. Kessel, G. Schierning, J. Räthel, and M. Herrmann, "Field-Assisted Sintering Technology/Spark Plasma Sintering: Mechanisms, Materials, and Technology Developments," *Adv. Eng. Mater.*, **16** [7] 830-49 (2014).
29. Z. Munir, U. Anselmi-Tamburini, and M. Ohyanagi, "The Effect of Electric Field and Pressure on the Synthesis and Consolidation of Materials: A Review of the Spark Plasma Sintering Method," *J. Mater. Sci.*, **41** [3] 763-77 (2006).
30. Z. A. Munir, D. V. Quach, and M. Ohyanagi, "Electric Current Activation of Sintering: A Review of the Pulsed Electric Current Sintering Process," *J. Am. Ceram. Soc.*, **94** [1] 1-19 (2011).
31. M. Nygren and Z. Shen, "On the Preparation of Bio-, Nano-, and Structural Ceramics and Composites by Spark Plasma Sintering," *Solid State Sci.*, **5** [1] 125-31 (2003).
32. S. Wang, L. Chen, T. Hirai, and Y. Kang, "Microstructure Inhomogeneity in Al₂O₃ Sintered Bodies Formed During the Plasma-Activated Sintering Process," *J. Mater. Sci. Lett.*, **18** [14] 1119-21 (1999).

33. G. Xie, O. Ohashi, K. Chiba, N. Yamaguchi, M. Song, K. Furuya, and T. Noda, "Frequency Effect on Pulse Electric Current Sintering Process of Pure Aluminum Powder," *Mater. Sci. Eng., Proc. Conf.*, **359** [1-2] 384-90 (2003).
34. H. Tomino, H. Watanabe, and Y. Kondo, "Electric Current Path and Temperature Distribution for Spark Sintering," *J. Jpn. Soc. Powder Powder Metall.*, **44** [10] 974-9 (1997).
35. U. Anselmi-Tamburini, S. Gennari, J. Garay, and Z. A. Munir, "Fundamental Investigations on the Spark Plasma Sintering/Synthesis Process: II. Modeling of Current and Temperature Distributions," *Mater. Sci. Eng., Proc. Conf.*, **394** [1] 139-48 (2005).
36. X. Wang, S. Casolco, G. Xu, and J. Garay, "Finite Element Modeling of Electric Current-Activated Sintering: The Effect of Coupled Electrical Potential, Temperature and Stress," *Acta Mater.*, **55** [10] 3611-22 (2007).
37. S.-X. Song, Z. Wang, and G.-P. Shi, "Heating Mechanism of Spark Plasma Sintering," *Ceram. Int.*, **39** [2] 1393-6 (2013).
38. R. Dohedoe, G. West, and M. Lewis, "Spark Plasma Sintering of Ceramics: Understanding Temperature Distribution Enables More Realistic Comparison with Conventional Processing," *Adv. Appl. Ceram.*, **104** [3] 110-6 (2005).
39. E. A. Olevsky and L. Froyen, "Impact of Thermal Diffusion on Densification During SPS," *J. Am. Ceram. Soc.*, **92**, S122-S32 (2009).
40. U. Anselmi-Tamburini, J. E. Garay, and Z. A. Munir, "Fundamental Investigations on the Spark Plasma Sintering/Synthesis Process III: Current Effect of Reactivity," *Mater. Sci. Eng., Proc. Conf.*, **407** [1-2] 24-30 (2005).
41. E. A. Olevsky, C. Garcia-Cardona, W. L. Bradbury, C. D. Haines, D. G. Martin, and D. Kapoor, "Fundamental Aspects of Spark Plasma Sintering: II. Finite Element Analysis of Scalability," *J. Am. Ceram. Soc.*, **95** [8] 2414-22 (2012).
42. M. Koide, S. Takei, T. Sato, and K. Matusita, "Preparation of Silica Glass by Pulsed Electric Current Method," *J. Ceram. Soc. Jpn.*, **110** [1285] 867-9 (2002).

43. T. G. Mayerhöfer, Z. Shen, E. Leonova, M. Edén, A. Kriltz, and J. Popp, "Consolidated Silica Glass from Nanoparticles," *J. Solid State Chem.*, **181** [9] 2442-7 (2008).
44. B. Barazani, D. Torikai, and C. K. Suzuki, "Study of Vitreous Silica Sintering by Spark Plasma (SPS)," *Proceedings of the 21st Brazilian Congress of Mechanical Engineering*. Natal, RN, Brazil (2011).
45. D. Torikai, B. Barazani, E. Ono, M. Santos, and C. Suzuki, "Quartz Crystal Reinforced Silica Glass Obtained by Spark Plasma Sintering," *J. Aust. Ceram. Soc.*, **49** [1] 9-14 (2013).
46. J. Zhang, R. Tu, and T. Goto, "Fabrication of Transparent SiO₂ Glass by Pressureless Sintering and Spark Plasma Sintering," *Ceram. Int.*, **38** [4] 2673-8 (2012).
47. X. Zhang, X. Yu, B. Zhou, W. Luo, W. Jiang, W. Jiang, Z. Shen, and L. Wang, "Sinterability Enhancement by Collapse of Mesoporous Structure of SBA-15 in Fabrication of Highly Transparent Silica Glass," *J. Am. Ceram. Soc.*, **98** [4] 1056-9 (2015).
48. L. Shi, L. Wang, W. Jiang, and W. Luo, "Preparation of Highly Transparent Silica Glass by SPS Sintering of SBA-15," *Mater. Sci. Forum.*; **848**, 312-318 (2016).
49. P. Dibandjo, L. Bois, C. Estournes, B. Durand, and P. Miele, "Silica, Carbon and Boron Nitride Monoliths with Hierarchical Porosity Prepared by Spark Plasma Sintering Process," *Microporous Mesoporous Mater.*, **111** [1] 643-8 (2008).
50. H. Maheshwari, J. D. Roehling, B. A. Turner, J. Abdinor, T. B. Tran-Roehling, M. D. Deo, M. H. Bartl, S. H. Risbud, and K. van Benthem, "Robust Mesoporous Silica Compacts: Multi-Scale Characterization of Microstructural Changes Related to Physical–Mechanical Properties," *J. Mater. Sci.*, **51** [9] 4470-80 (2016).
51. M. Röding, L. Del Castillo, M. Nydén, and B. Follink, "Microstructure of a Granular Amorphous Silica Ceramic Synthesized by Spark Plasma Sintering," *J. Microsc.*, **264** [3] 298-303 (2016).

52. V. A. Drits and C. Tchoubar, *X-Ray Diffraction by Disordered Lamellar Structures: Theory and Applications to Microdivided Silicates and Carbons*. Springer Science & Business Media, Berlin, DE, 2012.
53. M. Treacy, J. Newsam, and M. Deem, "A General Recursion Method for Calculating Diffracted Intensities from Crystals Containing Planar Faults," *Proc. R. Soc. Lond. A*, **433** [1889] 499-520 (1991).
54. L. Ramond, G. Bernard-Granger, A. Addad, and C. Guizard, "Sintering of Soda-Lime Glass Microspheres Using Spark Plasma Sintering," *J. Am. Ceram. Soc.*, **94** [9] 2926-32 (2011).
55. M. Wojdyr, "Fityk: A General-Purpose Peak Fitting Program," *J. Appl. Crystallogr.*, **43** [5 Part 1] 1126-8 (2010).
56. A. Coelho, *Topas 4.2 Technical Reference*. Bruker Corporation, Billerica, MA, 2009.